UNIVERSITÀ DEGLI STUDI DI FIRENZE
Dipartimento di Astronomia e Scienza dello Spazio
Area disciplinare FIS05
Scuola di dottorato in Astronomia
Ciclo XX

Study and Characterization of the Pyramid Wavefront Sensor for Co-phasing.

Candidato: Dott. Enrico Pinna

Tutore: Dott. Simone Esposito

Cotutore: Prof. Alberto Righini

Coordinatore: Prof. Claudio Chiuderi

Contents

Chapter 1

Introduction

1.1 ELTs

The actual class of large IR/optical telescopes is the $8 - 10\,m$ class, that started the operations in 1993 with the *KeckI*, then *KeckII* and the four UT of the *Very Large Telescope*. These two facilities have been followed by the two *Gemini*, the *Subaru* and, more recently, by the *Large Binocular Telescope*. Soon the *Gran Telescopio de Canarias* will become operational. At the same time, during the last years of the XX century and the firsts of the XXI, the IR/optical large telescope panorama has been populated by a number of projects for the next generation of ground-based telescopes. These projects have been characterized by having the diameter size in the range $20 \div 100\,m$ and have been identified with the acronym ELT: *Extremely Large Telescopes*. In the first design phase the projects were:

- California Extremely Large Telescope (CELT - USA) [1]
- Euro 50 (Sweden) [2]
- Japanese Extremely Large Telescope (JELT - Japan) [3]

- OverWhelmingly Large telescope (OWL - Europe) [4]
- Giant Segmented Mirror Telescope (GSMT - USA) [5]
- Very Large Optical Telescope (VLOT - Canada) [6]

With time passing, the project population evolved with merging of different projects and resizing of telescope design. Three projects passed this critical phase and are now on the road for the realization: the European-ELT (Europe), the Thirty Meter Telescope (USA/Canadian consortium) and the Great Magellan Telescope (USA). We are now going briefly through these three projects illustrating the ELT basic parameters relevant for the work of this thesis.

The *European Extremely Large Telescope* (E-ELT)

The OWL project has been reviewed in 2006 with the final choice to scale the primary mirror diameter from the original size of $100\,m$ to the range $30 \div 60\,m$. This review process ended in 2007 with the definition of the E-ELT project as a $42\,m$ telescope [7] (fig. 1.1). The realization phase is foreseen to start in 2010 and operations are scheduled for 2017. The actual optical design (fig. 1.1 bottom) does not follow a classical scheme: is a 5 mirror configuration employing 3 powered mirror in order to improve the optical correction over a larger field ($10'X10'$ diffraction limited), with a wavelength coverage ranging from the near UV to the far infrared (0.32 to $20\,\mu m$). The primary mirror will be highly segmented and aspherical, composed by more than 1000 segments of $1.22\,m$ flat-to-flat.

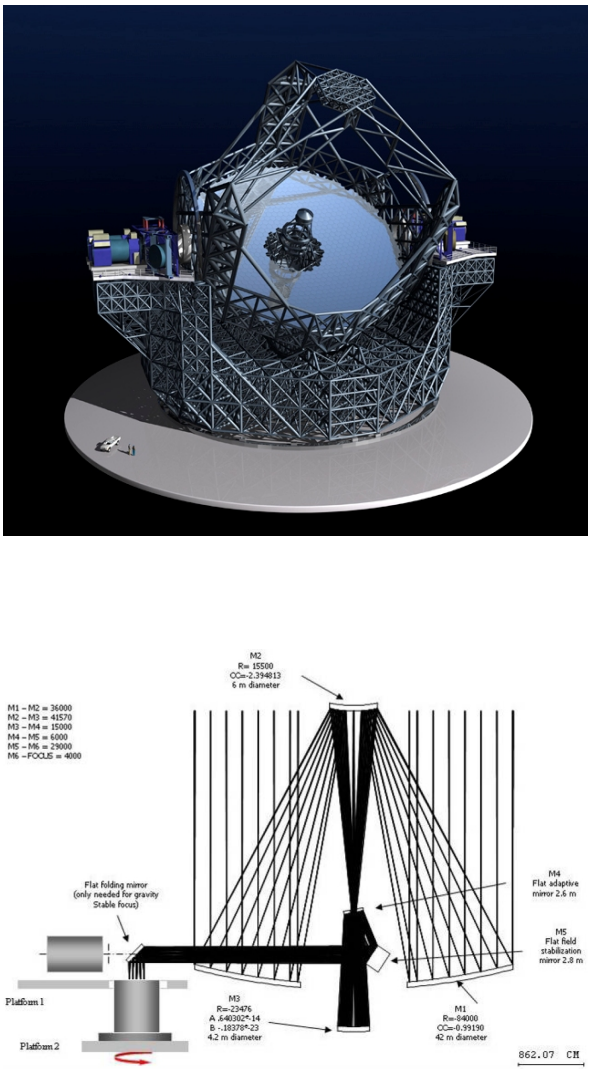

Figure 1.1: **Top:** pictorial view of E-ELT. In the bottom left corner the car and human figures give the scale of its $42\,m$ primary mirror. **Bottom:** A schematic of the non conventional optical design of E-ELT. Let's notice the the fourth and fifth mirrors in the optical train, these will provide the adaptive optics correction.

The *Thirty Meter Telescope* (TMT)

TMT [8] will be a wide-field, Ritchey-Chretien telescope with a 492 segment, 30 meter diameter primary mirror, a fully active secondary mirror and an articulated tertiary mirror. TMT construction will start in 2009 with the goal of testing the telescope with its full primary mirror in 2016.

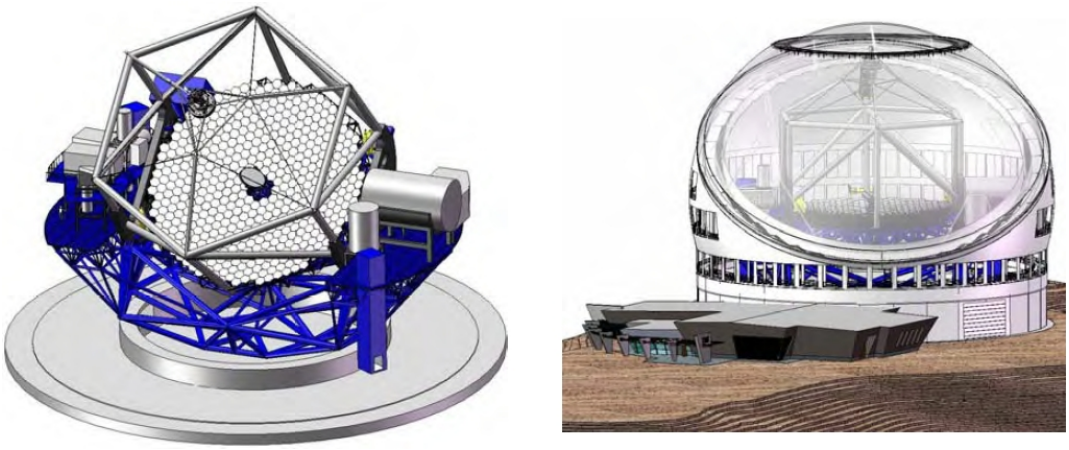

Figure 1.2: The TMT project. The telescope mounted on its structure (**left**) and the spherical dome (**right**).

The *Giant Magellan Telescope* (GMT)

The GMT [9] present an unique design in the ELT's panorama. The optical configuration is Gregorian with a primary mirror (see fig. 1.3 left) composed by six off-axis $8.4\,m$ circular segments that surround a central on-axis segment, forming a single optical surface with a collecting area equivalent to a filled aperture 21.4 meters in diameter. This design is offering the minimum segmentation in the ELT class. Moreover, the GMT secondary mirror (see fig. 1.3 right) is composed by seven thin adaptive shells. Each shell is mapping to a single primary mirror segment. This choice allows to compensate

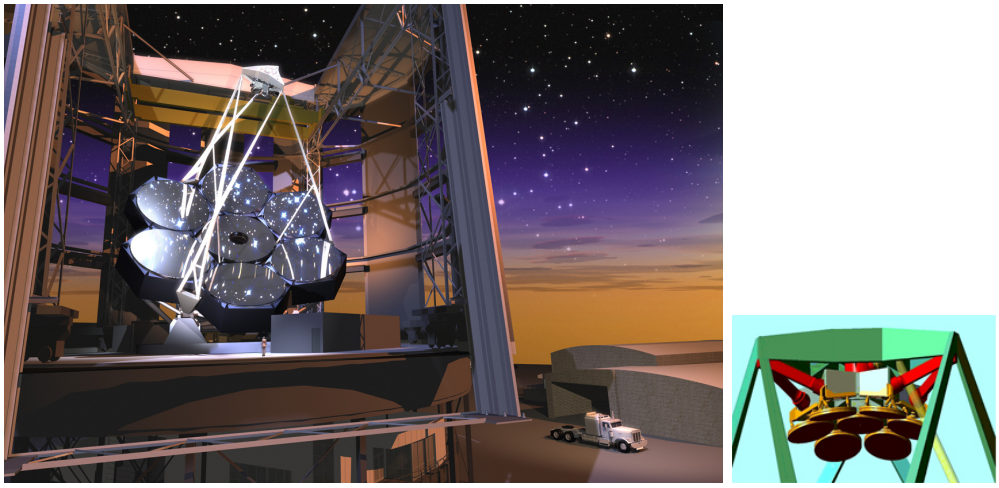

Figure 1.3: **Left:** pictorial view of the Great Magellan Telescope. The primary is composed by 7 segments having diameter of $8\,m$. **Right:** the GMT secondary mirror composed by 7 adaptive shells that will provide the adaptive optics correction.

the primary segment misalignments with the fast secondary segments.

1.2 Co-phasing the ELT's primary mirrors

1.2.1 The segments control system

In the variety of optical configurations of the ELT project, the common element is the primary segmentation, from the 7 up to the 1000 segments for GMT and E-ELT respectively. The segmentation allows enlarging the telescope diameter, but, on the other hand, introduces the problem of the segments control. The segments have to reproduce the ideal optical surface in order to achieve an optical quality equivalent to the correspondent monolithic one. The optical performances are sensitive to three of the rigid body degrees

of freedom of each segment: **piston, tip and tilt**. These are *out-of-plane* motions. It is not very sensitive to the other three degrees of freedom: *X and Y translation* and *clocking* rotation about the center. These are *in-plane* motions. Therefore, the support system controls the in-plane motions passively and controls the out-of-plane motions actively. Each segment has three actuators that allow it to be **aligned** (in *tip&tilt*) and **phased** (in *piston*) to form an accurate, continuous surface. The solution adopted by all the ELT projects [10] is a closed-loop that control the three actuators using as feed-back the signal produced by capacitive sensors [11] positioned on the edges between the segments. As example, the TMT actuator and capacitive sensor and their arrangement on the segment [12] are shown in fig. 1.4.

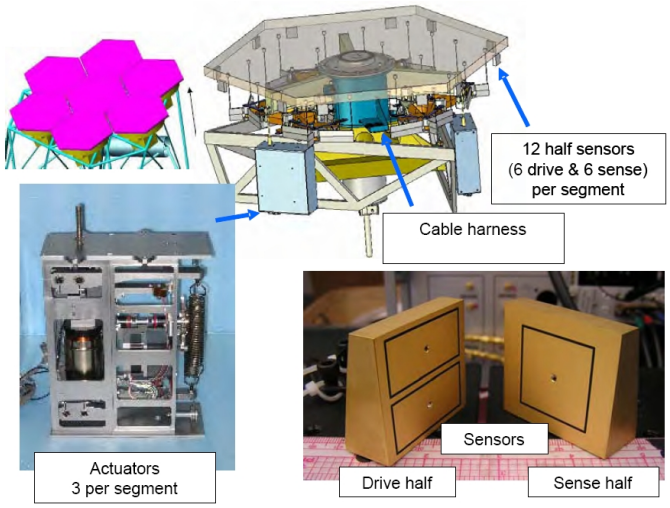

Figure 1.4: The segment actuator (**bottom-left**) and the capacitive sensor (**bottom-right**) developed for the TMT primary mirror segments. Their arrangement in the segment structure is shown in a pictorial view (**top**).

We focalize our attention now on the phasing problem, trying to quantify the required accuracy for the phasing of the primary mirror. The relationship

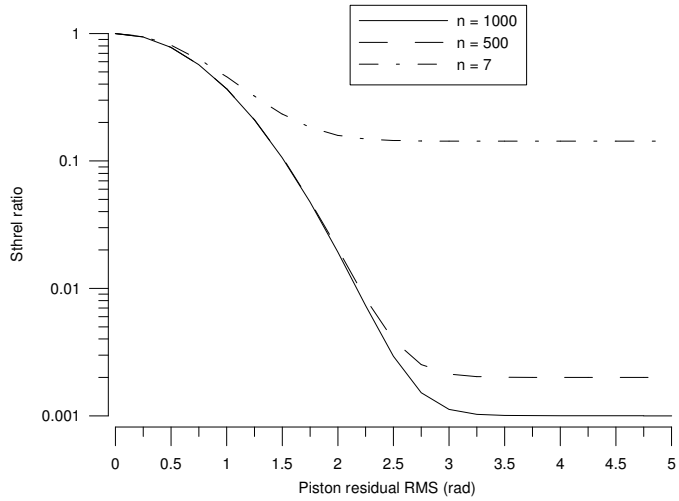

Figure 1.5: The Sthrel ratio of a perfect optical system having the pupil composed by n segments and affected only by the piston error.

between the residual piston error (σ) and the Sthrel ratio (SR) has been identified by Chanan and Troy in 1999 [13] and is described by the equation:

$$SR = \frac{1 + e^{-\sigma^2}(n-1)}{n} \tag{1.1}$$

In our case the SR is the ratio between the maxima of the ideal telescope with a primary composed by n segment having residual piston error σ, and the perfectly phased one. In fig. 1.5 eq. 1.1 is plotted for the cases $n = 7, 500, 1000$. For $\sigma \to \infty$, eq.1.1 says that the SR is reduced of a factor n, that means our telescope, in term of Sthrel, behaves as a single segment. Fig. 1.5 says that, in practice, this happen in the range $\sigma = 2 \div 4\, rad$ depending on n. Now, if we want to know the required phasing accuracy, we have to ask the required SR or residual wavefront error. This number, of course varies with the different astronomical applications. All ELTs will have an adaptive optic system that will correct the atmospheric turbulence achieving different

performances depending on the instrument requirement. The extremes are represented by GLAO (*Ground Layer Adaptive Optics*), that provide just a seeing improvement over a large field, and the XAO (*eXtreme Adaptive Optics*, that will provide on axis high contrast images.

The GLAO systems perform a partial turbulence correction over a wide field (scientific FoV $\geq 1 arcmin$). This partial correction typically provide an improvement in angular resolution of a factor 2, so we can take $\theta_{GLAO} = 0.2 \div 0.5\, arcsec$. From θ_{GLAO} we can estimate the wavefront spatial coherence as $r_0(GLAO) = \lambda/\theta_{GLAO}$. If $r_0(GLAO)$ is smaller or comparable to the diameter of the single primary segment ($\sim 1\, m$ for E-ELT and TMT), is clear that the diffraction effects of the residual phasing error will not affect the telescope performances. When the working λ increases, so do $r_0 \propto \lambda^{6/5}$ becoming comparable with the segment size. As example, the GLAO performances in K band are foreseen to achieve a $SR \sim 0.1$. This value, used in eq. 1.1, gives us the corresponding residual piston rms of $\sim 500\, nm$. Therefore, the piston error has to be a fraction (let's say $100\, nm$) of this value in order to not limit the telescope optical quality.

The opposite case is when an high-order adaptive optics system is correcting the atmospheric turbulence achieving the diffraction limited resolution. The requirement is that the residual phasing error does not degrade the image quality. We can have a quick estimation of this error budget considering the residual wavefront error of an high-order ideal[1] adaptive optics system. Taking in to account an actuator pitch (projected on the primary mirror) of $25cm$, we found with the classical computation [14], a wavefront residual rms of $25\, nm$ (this is the error budget estimate for the TMT working in high-

[1]With *ideal* we mean that the wavefront is perfectly detected and the correction is applied instantaneously.

order adaptive optics correction [8]). This number says that the acceptable phasing error has to be a fraction of this error budget, let's say $\sim 5\,nm$ rms.

We can summarize by saying that the **phasing accuracy** required for the ELTs is between 5 and $100\,nm$ rms on the wavefront that become $2.5 \div 50\,nm$ on the mirror surface.

Another requirement for the ELT phasing is the **capture range** on the differential piston error. This quantity is defined as the maximum piston error that can be corrected by a given phasing system. This capture range defines the accuracy of the segment mechanical integration, it is easy to understand how a required accuracy of $1, 10$ or $100\,\mu m$ has different impact in terms of instrumentation and time required for the mechanical integration. In the ELT case the complete aluminization of the primary once per year requires the daily substitution of one or more segments. Therefore the time required by each single segment integration has an impact on the daily telescope schedule.

1.2.2 The Phasing sensors

Now we know the required accuracy for the phasing, let's come back to the phasing and alignment system. The capacitive sensors measure the relative positions of the adjacent edges, this is an effective system to keep the segment relative positions stable. However, these positions have to be calibrated respect to the ideal optical surface. This is the duty of the *Phasing WaveFront Sensor* (PWFS) that calibrates the segment positions analyzing the wavefront generated by a reference source and reflected by the segmented mirror. The word *phasing* underline that this device is not a standard wavefront sensor (WFS). The usual WFS's duty is the measurement of the wavefront

continuous aberrations [2], so the segment tip&tilt, introducing a local finite slope on the wavefront, are measured by standard WFSs; on the other hand, the pure differential piston generates only phase steps. So, a PWFS is commonly indicating an optical sensor able to measure the differential piston.

The phasing sensor at Keck telescopes

Up to now, the unique cases of active segmented primary mirrors for optical/IR telescopes is represented by KeckI and KeckII. We briefly illustrate here the differential piston detection as done routinely at Keck telescopes [15] [16], because represent the natural reference for comparison with new techniques. The phasing sensor at Keck is called PCS [17] and is a Shack-Hartmann type wavefront sensor, which is permanently mounted at the left bent Cassegrain focal station of the Keck telescope. The key element is an array of $2\,mm$ X $3\,mm$ prisms, which replaces the usual lenslet array in a traditional ShackHartmann camera. This prism array is preceded by a mask at the position of the exit pupil. The mask, at a scale of $1/200$ of the primary mirror, defines small circular sub-apertures ($\sim 12\,cm$ in diameter referred to the primary) at the center of each of the 84 intersegment edges see fig. 1.6 on the left). The diffraction pattern produced on the focal plane by each lenslet is function of the phase step present on the sub-aperture. The coefficients of the correlation between the measured pattern and a set of theoretical ones (see fig. 1.6 on the right) determines the edge steps best estimation. Then all the measured step are considered for the estimation of the differential piston error obtained through a singular value decomposition process.

Let's now consider the problem of the light source. The PWFS detects the mirror differential pistons analyzing the optical path differences introduced

[2] As required in order to drive adaptive optics system.

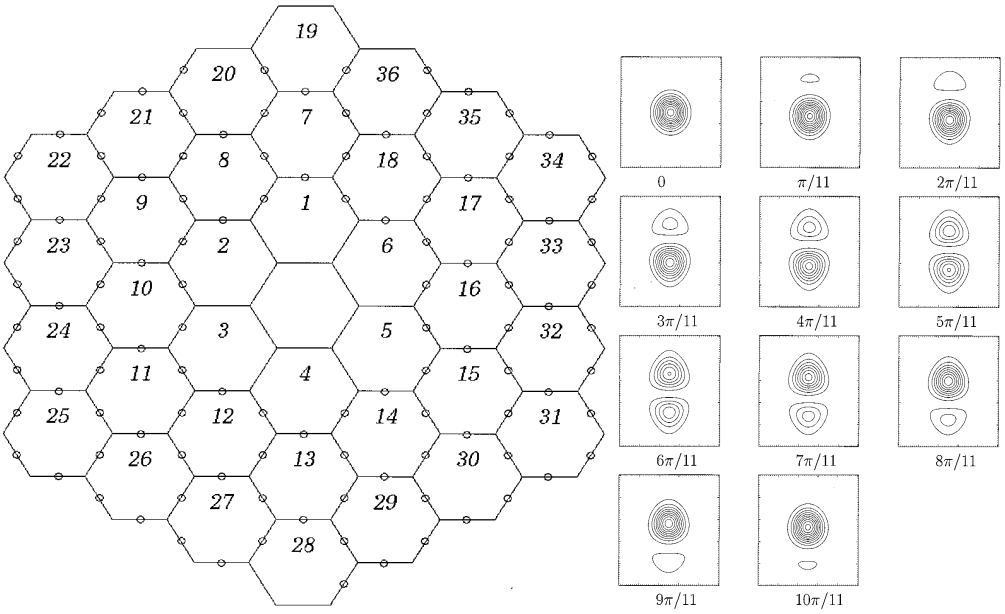

Figure 1.6: **Left:** geometry of the primary mirror of the Keck telescopes, showing the 78 circular sub-apertures that sample the intersegment edges in the phasing procedure. Each segment is $0.9\,m$ on a side. The sub-apertures, projected on the primary, are $12\,cm$ in diameter. **Right:** theoretical diffraction patterns (monochromatic light) for a sub-aperture with a physical step $\pi a/11$. The pattern represented are for $a = 1, 2, 3, ..., 11$.

by segment displacements on a reference wavefront. Of course, this wavefront has to uniformly illuminate the entire primary mirror. The implementation of a reference source internal to the telescope optical train poses serious technical difficulties as the access of the primary mirror center of curvature that is located above the dome (tens of meters in the ELT case). So all the PWFS are supposed to use a **natural guide star** as reference source. That is the reason of the small size of the PCS sub-apertures. The patterns shown in fig. 1.6 are generated by diffraction effects on the PCS sub-aperture. In order to reach the diffraction limit in presence of atmospheric turbulence, the sub-aperture size has to be smaller than the atmospheric coherence length r_0 that is typically $15 \div 20\, cm$ at the sensing wavelength $0.5 - 0.8\, \mu m$. So, the PCS strategy is to work with spatial frequencies that are not affected by the atmospheric turbulence.

The PCS technique has several limitations, one for all the critical alignment of the pupil mask that become greater with the increase of the segment number.

Some new co-phasing techniques has been proposed at the beginning of years 2000 together with the born of the ELT projects. Starting from 2005, in Europe, a selection of phasing sensor is under experimental study in the APE project.

1.3 The *Active Phasing Experiment* (APE)

APE is a work-package of the Extremely Large Telescope Design Study (ELT-DS), that is a technology development programme sponsored by the European Commission within Framework Programme 6. The ELT-DS has been divided in the various technological areas and APE is part of the Wavefront

Control task. The APE objective [18] is the design, construction and test in laboratory and on-sky of various PWFSs performing active wavefront control with a segmented mirror. APE will compare the performances of four different phasing sensors:

- SHAPS [19], derived from the Shack-Hartmann WFS
- ZEUS [20], based on the phase contrast interferometer
- DIPSI [21], a curvature WFS
- PYPS, a pyramid WFS for the co-phasing, that is the main subject of this thesis (chapter 3)

All these WFSs will be placed on the APE main bench represented in fig. 1.7. Here the system pupil is imaged on the *Active Segmented Mirror* (ASM [22], shown in fig. 1.8), simulating the optical effect of a segmented primary mirror. The ASM is a plane mirror composed by 61 hexagonal elements, each of those is controllable in piston and tip&tilt with three piezo-stacks with $\pm 7\,\mu m$ of mechanical stroke. The capacitive sensors, that are supposed to drive the actuators on the back of the ELT primary mirror segments, are emulated by an *Internal Metrology* (APE-IM) [23], that is an interferometer able to measure the segment piston errors working with two different wavelengths and the two linear polarizations. So that, the APE-IM will control the ASM segments in a fast closed-loop ($8\,HZ$) avoiding the piezo-stack drifts and correcting the hysteresis, typical for these devices. The WFSs will correct the segments phasing through the atmospheric turbulence averaging its disturbance in tens of seconds. During the tests in the ESO labs, foreseen to start in April 2008, the atmospheric turbulence will be simulated with MAPS [24], a multi-layer turbulence generator built and tested for the multi

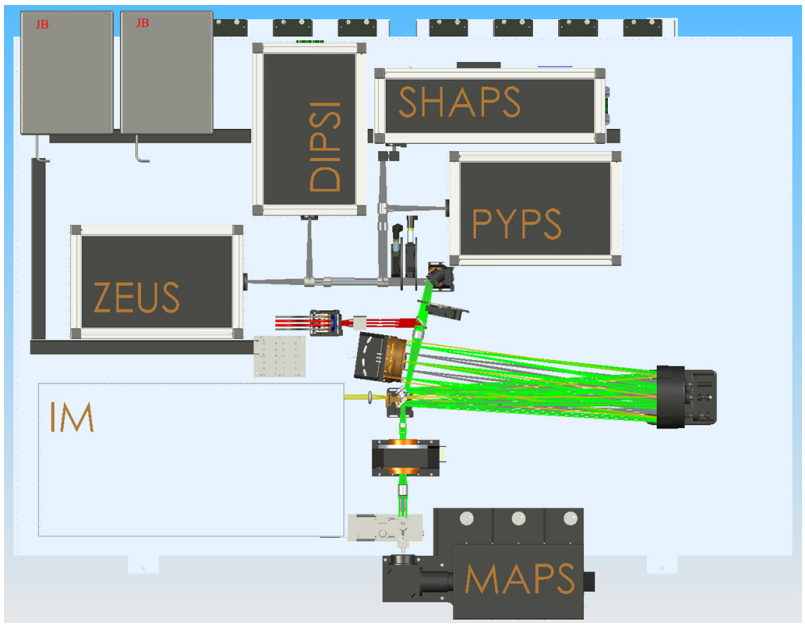

Figure 1.7: The opto-mechanical sketch of the APE bench. The turbulence simulator MAPS (on the bottom) is the system light source. The light pass through the field rotator, then the system pupil is imaged on the ASM (center). Afterwards the beam is split in order to feed the four phasing sensors: SHAPS, PYPS, ZEUS and DIPSI.

conjugated adaptive optic systems. After six months of test at the ESO Headquarter, the APE bench will be moved at a Nasmyth focus of the VLT UT3 where it will be offered, using a natural guide star, a real atmosphere and a real $8\,m$ telescope optical train.

The key parameter to evaluate the phasing techniques will be:

- the **final accuracy**, characterized by the residual wavefront rms;

- the **capture range**, that is the maximum differential piston that can

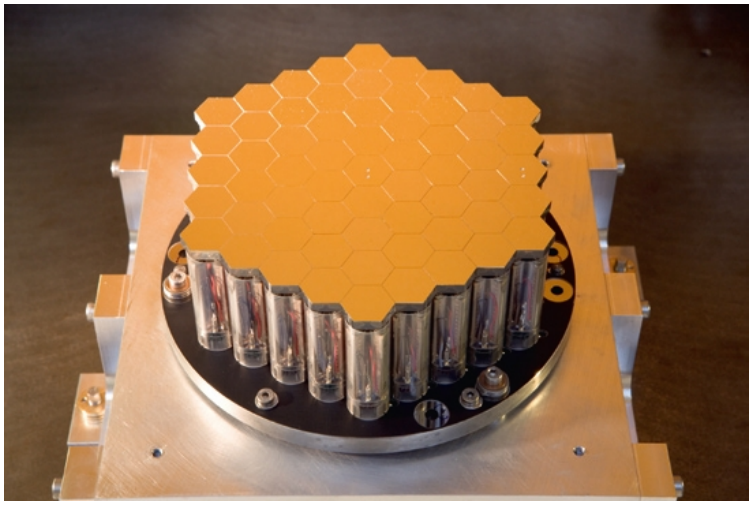

Figure 1.8: The Active Segmented Mirror completely assembled and ready to be installed on the APE bench.

be recovered by the WFS[3];

- the **operational time**, that include the required time to calibrate and close the phasing loop with the WFS;
- the **limiting star magnitude**, that is the maximum magnitude of the natural guide star that the WFS can use to achieve the required accuracy in the phasing.

1.4 The Pyramid Wavefront Sensor

The ability of the pyramid wavefront sensor to do phasing and alignment of mirror segments at the same time has been shown in 2001 using numerical simulations [25]. In the period 2000-2004 the Arcetri AO Group developed

[3]The phase ambiguity problem, illustrated in sect. 2.3, is a common problem for all the WFSs that detect the phase steps

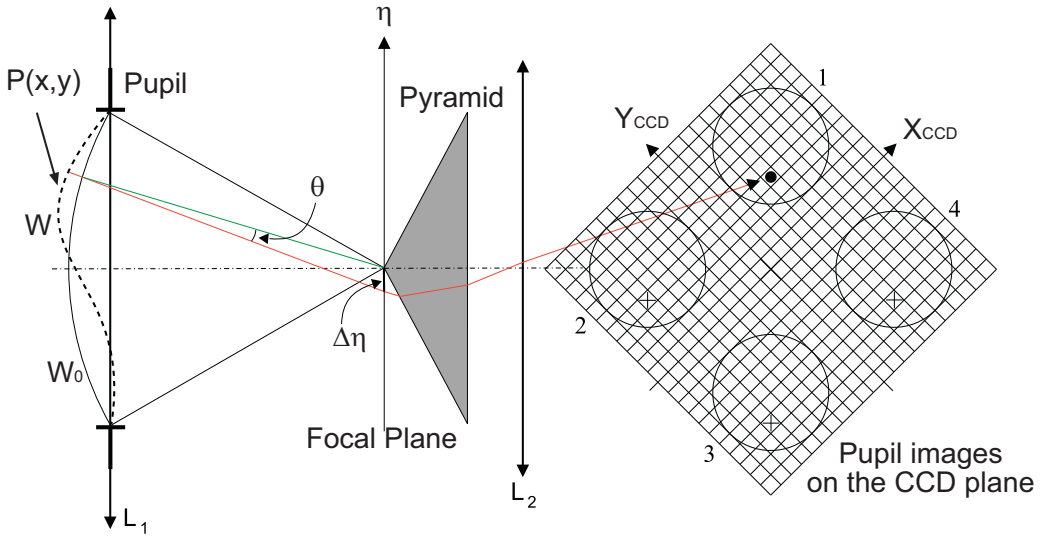

Figure 1.9: A scheme of the working principle of pyramid wavefront sensor.

this concept and has built a lab prototype of the PYramid Phasing Sensor (PYPS) [26]. In this section we introduce the pyramid wavefront sensor, while its application to the phasing will be analyzed in the next chapter

The PWS has been proposed by R. Ragazzoni in 1996 [27] and its working principle is derived from the well known Foucault test [28] for optical shop testing [29]. In this sensor, differently from the knife edge test, the spatial filtering is done by the four edges of the top surface of a square glass pyramid. As shown in fig.1.9, when a unaberrated converging beam (W_0) hits the vertex of the pyramid, the light is split in four identical beams, then four pupil images are generated through the camera lens (L_2) on the CCD plane. When the analyzed beam presents some aberration (W) in the (x, y) point of the pupil plane, then the ray propagating from this sub-aperture tilts of an angle θ. So, in the focal plane, this ray hits the pyramid at a distance $\delta\eta$ from the vertex illuminating only one of the four faces. In this case only one of the four pupils in the CCD plane receives light in the (x, y) region. Which pupil

receives the light in (x, y) reveals the signs of the local X and Y derivatives of the wavefront in this pupil sub-aperture. From the above description its easy to understand that the sub-apertures of a PWS are defined by the CCD pixels on each of the four pupils. PYPS is a PWS with tip&tilt modulation, this kind of sensor presents an optical configuration as shown in Figure 3-3, where, respect to Figure 3-2, a fast steering mirror is added in a plane conjugate to the exit pupil of the system in analysis. This device is driven so that the axis of the mirror describes a cone centered on the optical axis of the system; in this way the focus of an unaberrated beam is circling around the pyramid vertex, while an aberrated beam is circling around the point (dx,dy) as shown in Figure 3-4. The quantities dx and dy are directly proportional to the wavefront slopes. The intensities of the four pixels, associated with the pupil region (x,y), are proportional to the length of circumference arc that cross the corresponding pyramid face.

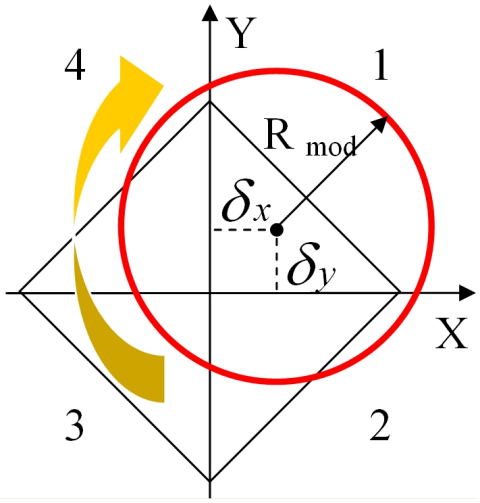

Figure 1.10: The effect in the focal plane of the fast steering mirror. The red circle is the path followed by an aberrated ray having in pupil x and y slopes that in the focal plane are translated in the displacement δ_x and δ_y.

Now we can define the X and Y signals of the PWS as:

$$S_x(x,y) = \frac{\Big(I_1(x,y) + I_4(x,y)\Big) - \Big(I_2(x,y) + I_3(x,y)\Big)}{I_{av}} \qquad (1.2)$$
$$S_y(x,y) = \frac{\Big(I_1(x,y) + I_2(x,y)\Big) - \Big(I_4(x,y) + I_3(x,y)\Big)}{I_{av}}$$

where (x,y) identify a sub-aperture in the pupil plane and the subscript i is relative to the four pupil images in the CCD plane. So, In(x,y) is the intensity of the pixel relative to the sub-aperture (x,y) in the nth pupil. I_{av} is the mean intensity on a single sub-aperture defined as:

$$I_{av} = \frac{N_{sub}}{\sum_{x,y}^{N_{sub}} \sum_{i=1}^{4} I_i(x,y)} \qquad (1.3)$$

When we say generally signal we mean the vector (Sx,Sy). In geometrical optic regime the relationships between the local derivatives on the wavefront and the PWS signals are given by

$$\frac{\partial W(x,y)}{\partial x} = \frac{R}{f}\sin(\frac{\pi}{2}S_x) \qquad (1.4)$$
$$\frac{\partial W(x,y)}{\partial y} = \frac{R}{f}\sin(\frac{\pi}{2}S_y)$$

these can be linearized around zero obtaining :

$$\frac{\partial W(x,y)}{\partial x} = \frac{R}{f}\frac{\pi}{2}S_x \qquad (1.5)$$
$$\frac{\partial W(x,y)}{\partial y} = \frac{R}{f}\frac{\pi}{2}S_y.$$

These equations demonstrate that the pyramid wavefront sensor is sensitive to the local first derivative of the wavefront.

Chapter 2

Pyramid Wavefront Sensor for co-phasing

In the last part of the previous chapter we introduced the PWS and its working principle in geometrical optics. This approach demonstrates the sensitivity of the PWS to the wavefront first derivative (eq. 1.5), allowing its use in adaptive optics systems and in the measurement of the primary segment tip and tilts. On the contrary, the detection of phase discontinuity by a PWS cannot be explained in geometrical optics regime. In order to explain in diffractive optics regime why our sensor is able to detect a phase step on the wavefront, we consider now the equations below, that quantifies the signals for sensor realized with two prisms[1] (with the edges aligned normally to the detection direction) when tip&tilt modulation is used and with a wavefront

[1]The two prisms equations differ from the pyramid equations only for the absence of the term representing the interference in between the four pupil images generated in the pyramid case. This term, analytically quite complex, add a contribution negligible in our argumentation.

phase $\phi(x, y)$ on the system pupil [30].

$$S_x(x_1, y_1) \propto |A_0| \int_{-B(y_1)}^{+B(y_1)} \frac{\sin[\phi(x, y_1) - \phi(x_1, y_1)]}{2\pi(x - x_1)} \frac{sin[a_{tt}(x - x_1)]}{x - x_1} dx \quad (2.1)$$
$$S_y(x_1, y_1) \propto |A_0| \int_{-B(x_1)}^{+B(x_1)} \frac{\sin[\phi(x_1, y) - \phi(x_1, y_1)]}{2\pi(y - y_1)} \frac{sin[a_{tt}(y - y_1)]}{y - y_1} dy$$

In these formulae S_x and S_y are the PWS signals as defined in 1.2, a_{tt} is the tip&tilt modulation amplitude in peak to valley phase-radians per pupil diameter and $B(x_1)$ is the y value of the pupil edge at $x = x_1$, while $B(y_1)$ is the x value of the pupil edge at $y = y_1$. The right term in the integral takes into account the modulation effect and is purely spatial being independent on the wavefront phase; this term is modulating the spatial distribution of the signal amplitude, varying with a_{tt} the sensor sensitivity to the wavefront slopes as well as the phase step as has been experimentally demonstrated in 2003 [26] [31]. On the other side, the modulation does not change the signal pattern characteristics as the dependence on the phase and the maxima and minima positions. Therefore, we will neglect this term in the rest of this chapter. The left term in the integral shows that the PWS signal is generated by the phase variations on the entire pupil across the considered direction (x or y). These phase variations contribute to the signal weighted by the inverse of the distance from the considered sub-aperture (x_1, y_1). It is easy to see from equation 2.1 that a phase discontinuity along the y axis will generate a x-signal as detailed below.

2.1 The PYPS signals

In this section we analyze the PYPS signal patterns due to a single segment piston or tip&tilt error in the monochromatic and colored cases. This analysis is done with analytical computation in some particular cases and with

simulations in the monochromatic case. All the results obtained in this section have been confirmed by the experimental signal patterns obtained during the PYPS acceptance test (sect. 3.2.2) and the WHT campaigns (sect. 4.2).

2.1.1 Piston signal

Pure monochromatic case

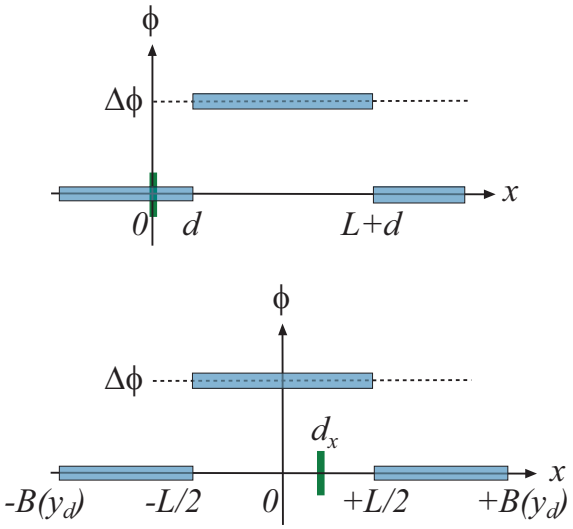

Figure 2.1: Schematic representation of a segment of size L with a phase piston error of $\Delta\phi$. **Top:** the sub-aperture taken into account (green line) is outside the segment surface at a distance d from the edge. **Bottom:** the sub-aperture is on the segment surface and the segment placed in the pupil center. The x values $-B(y_d)$ and $+B(y_d)$ represent the pupil boundaries.

We now consider a pupil with a square portion of side L affected by a pure differential piston $\Delta\phi$. We now analyze the signals of the two physically different cases for the sensor sub-aperture position, here the sub-aperture is considered infinitesimally extended in both the spatial directions. The first

case is when the sub-aperture is outside the segment; let it be at distance d along the x axis from the segment left edge (fig. 2.1 top.). Placing the pupil coordinate center on this sub-aperture and neglecting the TT modulation effect, the general equations 2.1 can be elementarily integrated and become:

$$\begin{aligned} S_X(0,0) &\propto \frac{\sin[\Delta\phi]}{2\pi}\int_d^{L+d}\frac{dx}{x} = \frac{\sin[\Delta\phi]}{2\pi}\ln\left[\frac{L}{d}+1\right] \\ S_Y(0,0) &= 0 \end{aligned} \tag{2.2}$$

or

$$\begin{aligned} s_X(0,0) &= 0 \\ s_Y(0,0) &\propto \frac{\sin[\Delta\phi]}{2\pi}\int_d^{L+d}\frac{dy}{y} = \frac{\sin[\Delta\phi]}{2\pi}\ln\left[\frac{L}{d}+1\right] \end{aligned} \tag{2.3}$$

when the sub-aperture is located at a distance d along the y axis from the segment bottom edge. The not null signals present two components: the left term is purely dependent on the segment piston error $\Delta\phi$, and defines the sinusoidal behavior of the signal amplitude with the phase error; the right term is dependent only by the sub-aperture position respect to the segment and denotes that the piston signal is relevant on the sub-apertures close to the segment edges.

In the second case we take into account when the sub-aperture is on the pistoned segment. We place now the pupil coordinate center in the center of the pupil that is also the segment center and the sub-aperture is at $(x = d_x, y = d_y)$ (fig. 2.1 bottom). Neglecting again the TT modulation

effect, the general equations 2.1 for this sub-aperture becomes:

$$\begin{aligned} S_X(d_x,d_y) &\propto \frac{sin[-\Delta\phi]}{2\pi}\int_{-B(d_y)}^{-\frac{L}{2}}\frac{dx}{x-d_x}+\frac{sin[-\Delta\phi]}{2\pi}\int_{+\frac{L}{2}}^{+B(d_y)}\frac{dx}{x-d_x}= \\ &= \frac{sin[\Delta\phi]}{2\pi}\ln\Big[\frac{(B(d_y)+d_x)(L/2-d_x)}{(B(d_y)-d_x)(L/2+d_x)}\Big] \\ S_Y(d_x,d_y) &\propto \frac{sin[-\Delta\phi]}{2\pi}\int_{-B(d_x)}^{-\frac{L}{2}}\frac{dy}{y-d_y}+\frac{sin[-\Delta\phi]}{2\pi}\int_{+\frac{L}{2}}^{+B(d_x)}\frac{dy}{y-d_y}= \\ &= \frac{sin[\Delta\phi]}{2\pi}\ln\Big[\frac{(B(d_x)+d_y)(L/2-d_y)}{(B(d_x)-d_y)(L/2+d_y)}\Big] \end{aligned} \tag{2.4}$$

The two terms of each signal are the contribution of the left and right or top and bottom segment edges for the x and y signals respectively. Its clear that S_x is null when $d_x = 0$ and, similarly, S_y when $d_y = 0$, because the sum of the two terms is zero, while, near the edges, the corresponding edge signals are dominating with respect to the others. Regarding the phase and spatial term of each of the two contributions, the considerations drawn in the first case remain valid.

The complete 2 dimensional signal patterns have been computed in numerical simulations[2] where the pyramid is considered as a phase screen in the focal plane and TT modulation is taken in to account. To show the agreement with the analytical computation, we considered a mirror with square segments having 2 rings of segments around the central one. Moreover the system pupil is defined as the circumference inscribed in the mirror. Fig.2.2 shows the piston signals for a segment entirely inside the pupil. This has been performed using a $2\lambda/D$ TT modulation and a pure monochromatic source. The patterns shown in fig. 2.2 are confirmed with the ones measured in lab represented in fig. 3.12 and 4.6.

[2]The simulation code used for the shown results has been written in IDL language by the author during the work for his degree thesis [31], then further developed by the Arcetri AO Group.

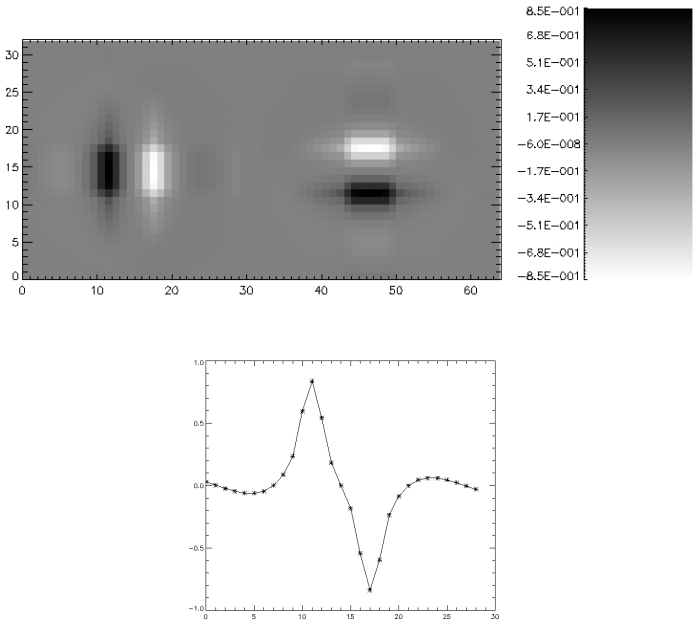

Figure 2.2: **Top**: the simulated $\mathbf{S_x}$ (left) and $\mathbf{S_y}$ (right) for a pure piston error ($\lambda/8$ wavefront) of a square segment with 6 sub-apertures per side. Each point in the plane represent an element of the signal vector $(\mathbf{S_x}, \mathbf{S_y})$ of numerical value corresponding to his greyscale tone. The position of the square segment edges are clearly identified by the signal maxima and minima. **Bottom**: the cut along the x axis of the $\mathbf{S_x}$ signal in the middle of the segment. The x position of the sub-apertures is represented in the horizontal axis, while the corresponding $\mathbf{S_x}$ values in the vertical.

The results obtained in this section can be summarized as follows. The PYPS signal generated by a differential piston error in the pupil is composed by: a **spatial term** that *localize the signal maxima and minima where there are the phase steps*; the **phase term** $S(\delta, \lambda) \propto \sin[4\pi\delta/\lambda]$ that denote the sine dependence on the phase step. This dependence has been experimentally demonstrated in 2003 [26].

Finite bandwidth case

When the light source has a finite bandwidth, the coherence length of the used beam plays a role and has to be taken into account in the analytical signal computation. In the signal expressions found in the previous section (eq.2.2, 2.3, 2.4), the only term dependent on λ is the phase term $sin[\Delta\phi]/(2\pi)$ that has to be integrated in $\delta\lambda$, taking into account all the contribution of the monochromatic components of the colored source. Two weight terms in the integral would be given by the CCD quantum efficiency and the spectrum of the source, both are taken equal to 1 for simplicity. So that, when the light has a finite bandwidth $\Delta\lambda = \lambda_2 - \lambda_1$, we have:

$$\begin{aligned} S(\delta,\lambda) \propto \int_{\lambda_1}^{\lambda_2} \sin\Big[4\pi\frac{\delta}{\lambda}\Big]d\lambda &= 4\pi\delta\int_{4\pi\delta/\lambda_2}^{4\pi\delta/\lambda_1}\frac{\sin[t]}{t^2}dt = \\ &= 4\pi\delta\Big[Ci(t) - \frac{\sin[t]}{t}\Big]_{4\pi\delta/\lambda_2}^{4\pi\delta/\lambda_1} \end{aligned} \tag{2.5}$$

where $Ci(t)$ is the cosine integral function and we used $t = 4\pi\delta/\lambda$. The function obtained in eq. 2.5 is represented for two bandwidth cases in fig. 2.3. This behavior can be easily understood considering that, when $\delta = 0$ all the $\Delta\phi$ are equal and all the signal contributions of the different $d\lambda$ are directly summed. When $\delta \neq 0$, the sine phases of each $d\lambda$ are different because $\Delta\phi = \Delta\phi(\lambda)$; e.g., when $\delta = \lambda_1\lambda_2/4(\lambda_2-\lambda_1)$ we obtain $\Delta\phi(\lambda_2)-\Delta\phi(\lambda_1) = \pi$ and the contribution of the signal due to λ_1 and λ_2 are equal in amplitude and opposite in sign, so they are cancelling each other.

The spatial terms remain unchanged with respect to the monochromatic case, so the 2 dimensional spatial patterns are the same as found in sect. 2.1.1.

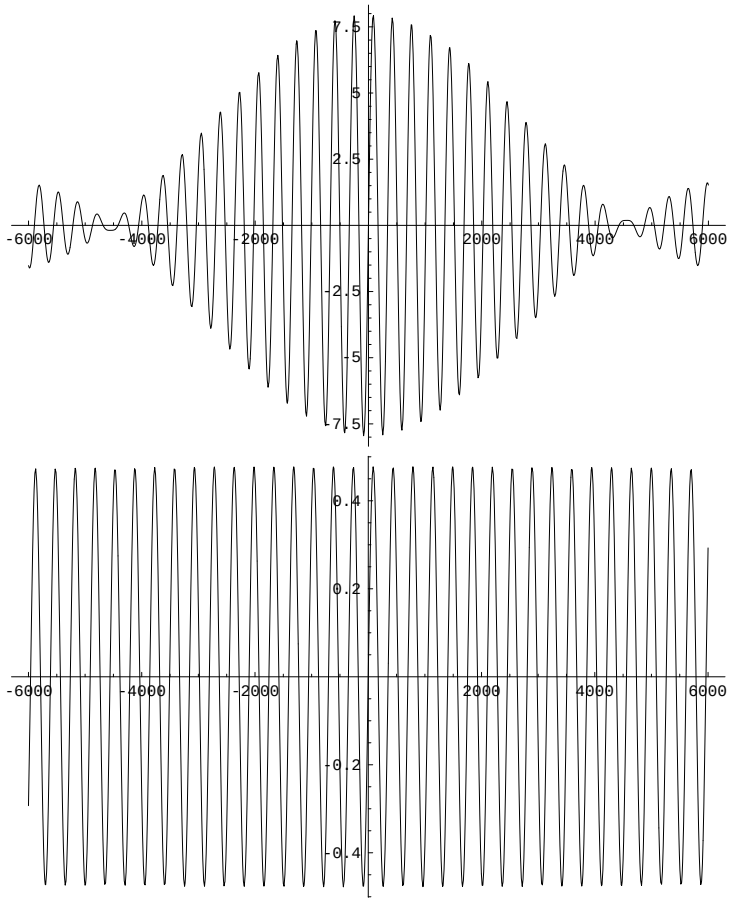

Figure 2.3: The phase step signal amplitude (vertical axis in arbitrary units) as function of the physical step δ (x axis in nanometer). These are the theoretical values obtained from eq.2.5 for the case of $\lambda_1 = 650\,nm$, $\lambda_2 = 700$ (**top**) and $\lambda_1 = 700\,nm$, $\lambda_2 = 703$ (**bottom**). Let's note that the minimum of the $50\,nm$ bandwidth case is $\sim 4550\,nm$, that corresponds to half (because of the factor 2 working in reflection) the coherence length of the beam $l_c = (\lambda_2 - \lambda_1)/\Delta\lambda = 9100\,nm$.

2.1.2 Tip&tilt signal

The segment tip or tilt signal pattern is due to two components: the slope on top the segment and the phase discontinuity at the edges. For the generic

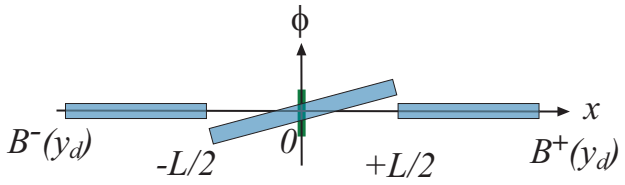

Figure 2.4: Schematic representation, as done in fig. 2.1 for the piston, of a segment of size L affected by a pure tilt error. The considered sub-aperture is taken in the the segment center. The wavefront experiences two equal phase steps at the segment borders, while on top of the segment the wavefront is simply tilted. B^- and B^+ are x values of the pupil border at $y = y_d$.

segment (not on the pupil border) let's consider the sub-aperture placed on the segment center (for simplicity we define here the axis origin $x = 0, y = 0$). For a pure tilt in the x direction we can write the analytical signal (neglecting again the tip&tilt modulation as done for the piston) using eq. 2.1:

$$\begin{aligned} S_x(0,0) &\propto \int_{-L/2}^{+L/2} \frac{\sin[4\pi\alpha x/\lambda]}{2\pi x} dx \sim \int_{-L/2}^{+L/2} 2\frac{\alpha}{\lambda} dx = 2\frac{\alpha}{\lambda} L \\ S_y(0,0) &= 0 \end{aligned} \tag{2.6}$$

Therefore, in the linear regime of the sine function, the x signal is directly proportional to the segment length and to its physical slope α. The linear dependence on the slope is in agreement with the known behavior in geometrical optics regime described in sect. 1.4. On this considered sub-aperture the phase steps at the segment edges do not give any contribution. On the contrary, the signal of the sub-apertures on the segment edges is generated

by the phase steps (see fig.2.4). The complete 2 dimensional signal patterns, as for the piston case, are obtained through simulations and represented in fig. 2.5. As shown in this pictures, the tip&tilt signals show up mainly in the

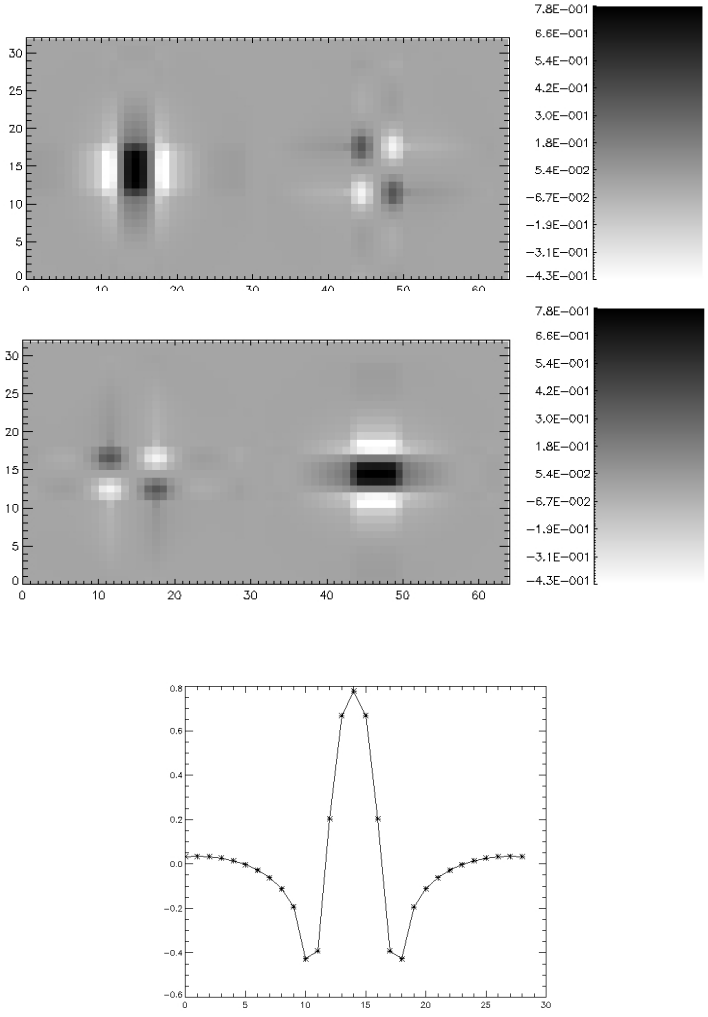

Figure 2.5: **Top:** the simulated signal pattern, represented as in fig.2.2, for a pure tilt in the horizontal direction of a square segment. **Center:** the signal pattern for the case of a pure tilt in the vertical direction. **Bottom:** the plot of the x part of the horizontal tilt signal across the middle of the segment.

x and y part of the sensor signal respectively. Both signals are symmetric

respect to the segment center. Moreover, the tip y signal and the tilt x signal have antisymmetrical patterns. Therefore, the tip&tilt signals result linearly independent in the signal space. Both signals are linearly independent from the piston signal, that presents an antisymmetrical pattern in the x and the y part of the signal. This is fundamental for the disentangling of the three degrees of freedom as we will demonstrate in the next section.

2.2 Piston and tip&tilt correction

One of the fundamental advantages that PYPS presents, with respect the other proposed phasing sensors [21] [20], is the ability to **detect and control piston and tip&tilt of all the segments in the pupil at the same time**. This is achieved thanks to the signal shapes seen in section 2.1 and the interaction matrix approach. Now we will see these two important aspects in detail.

2.2.1 Signal disentangling

Equations 2.1 are stating that the pyramid signal, as defined in eq. 1.2, is a linear combination of the phase aberrations encountered in the pupil itself. In particular sections 2.1.1 and 2.1.2 showed that the piston signal and the tip&tilt signals produced by a single segment are linearly independent. Assuming that a proper sampling is used, as detailed below, this property allows discriminating and measuring tip, tilt and piston out from a single signal pattern. Furthermore, the discrimination in between the segments is guaranteed by the different sets of sub-apertures involved in the signal pattern, because of the different spatial location in the pupil plane. Let's now consider the signal dependence on the phase step $\Delta\phi$ and on the segment tilt

α: as stated in sect. 2.1.1 and 2.1.2, these are respectively $S \propto \sin[\Delta\phi] \sim \Delta\phi$ and $S \sim \alpha/\lambda$ when $\Delta\phi$ and α are ~ 0, that corresponds to the perfectly phased and aligned position. In these conditions we have both *signal patterns*, piston and tip&tilt, that are *directly proportional in amplitude to the segment degree of freedom we want to correct*. We want to underline this point that is a peculiar property of PYPS for the piston detection with respect to Shack-Hartmann based [16] [19] and other phasing sensors [32] [21] [20] that require more complex data reductions[3] respect to the simple singal computation required by eq. 1.2. This PYPS characteristic allows us to consider the signal pattern, generated by the piston, tip&tilt errors of all the segments in the pupil, as a linear superposition of all the single signal patterns. So, in formulae, we can write a linear system for the sensor signals vector $\mathbf{S} = (S_x, S_y)$ like the following one:

$$S(j) = \sum_{i=1}^{N_s} a_{ij}\theta_{xi} + \sum_{i=1}^{N_s} b_{ij}\theta_{yi} + \sum_{i=1}^{N_s} c_{ij}p_i \tag{2.7}$$

where θ_{xj}, θ_{yj} and p are x tilt, y tilt and piston of the j-th segment respectively; $\mathbf{a}$, $\mathbf{b}$ and $\mathbf{c}$ are three vectors defining the sensor signals for a unit amplitude of the corresponding degree of freedom. Finally i is the segment index and j is the sub-apertures index. In this linear system the number of unknowns is 3 times the number of segments N_s, while the number of independent measurement is two times the number of sampling sub-apertures N_{sa}.

[3]We are referring to the pattern correlation required by the Shack-Hartmann based phasing sensors or to the signal profiles analysis required by sensors as the curvature ones.

2.2.2 Segment sampling

In this section we consider as first a segmented mirror composed by square segments because it matches the PYPS sub-apertures geometry defined by the pixel grid of the CCD detector. The number of sub-apertures has to be taken as low as possible when we are working with a noise limited CCD detector, as is the case with PYPS. To solve the equation system 2.7, the dimension of **S** has to be greater than the number of unknowns, so:

$$2N_{sa} \geq N_{DoF} \cdot N_s \tag{2.8}$$

where N_{DoF} is the number of degree of freedom to be measured for each segment. Because of the considered geometry we can only have: $N_{sa}/N_s = 1X1, 2X2, ..., nXn$. When we are interested only in the segment piston, the sampling $1X1$ satisfies eq. 2.8, while, when the estimation of piston and tip&tilt are required, eq.2.8 is satisfied starting from the sampling is $2X2$.

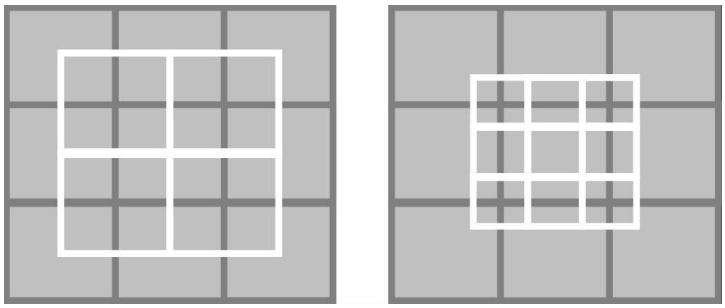

Figure 2.6: The arrangements of the sensor sub-apertures (white lines) with respect to the mirror segments (grey). The represented cases are the 1X1 sampling (**left**), allowing only the piston detection, and the 2X2 sampling (**right**), for the simultaneous detection of piston and tip&tilt of square segments.

We have to underline that the required sampling of 2X2 is a peculiar characteristic of the pyramid. This sampling is very low compared with the

ones required by the other phasing sensors, where the differential piston value is estimated fitting or cross-correlating the signals produced at each segment edge.

Considering now the hexagonal segment geometry, we have to say that is a really unlucky choice from the point of view of the sampling. That is because, in the pyramid case, the sub-aperture geometry is defined by the CCD pixel grid that is usually square or rectangular. As well known, the width height ratio of an hexagon is not rational, so we can not repeat the same sampling arrangement for all the mirror segments with a square grid of pixels. This problem could be solved with a CCD with rectangular pixels having the same ratio between width and height as the hexagon has. Anyway the availability of the Low-Light-Level CCDs, that solve the read out noise problem, allows to oversample the segments and deal with this not optimal arrangement. Moreover the 60^o geometry still does not match the 90^o one of the rectangular grid. In numerical simulation we verified that this mismatch does not affect the differential piston measurements; that is because the signal produced by the edges not aligned to the pixel grid is simply decomposed in S_x and S_y, so there is no information loss.

2.2.3 Piston and tip&tilt reconstruction and correction

Here we describe the algorithm that allows to compute the segment optical configuration from a given pattern of signals produced by PYPS. The developed algorithm is the *interaction/reconstruction matrix based process*, commonly used in Astronomical Adaptive Optics [33]. The Singular Value Decomposition algorithm [34] [35] provides an easy way to compute the vectors $\theta_{\mathbf{x}}$, $\theta_{\mathbf{y}}$ and $\mathbf{p}$ using the measured signals and a predetermined matrix

called reconstructor R. This matrix R is determined as follows. First the system interaction matrix M has to be identified. The M matrix is usually measured in lab but it can be derived form analytical computations or numerical simulations after some hypothesis are made about the considered system.

In order to measure M the usual process is recording the wavefront sensor signals produced by each system degree of freedom that has to be controlled. The matrix M is achieved arranging the signals as columns in the matrix. Considering how M is made up, it is easy to see that $\mathbf{S} = M\mathbf{C}$ where $\mathbf{C}$ is a command vector containing a set of values for the system degree of freedom. This leads in turn to $\mathbf{C} = M^{-1}\mathbf{S}$ where M^{-1} is the so called pseudo inverse of M achieved using the SVD algorithm. Now, assuming $R = M^{-1}$, we get $\mathbf{C} = R\mathbf{S}$. This matrix multiplication algorithm is quite useful in operating an iterative process, because a single matrix multiplication allows to pass from sensor signal to phase aberrations or, in other words, mirror commands. We point out that the use of an over determined system, that is always the case when we use the 2x2 pixel sampling scheme, allows to reduce the noise propagation error in solving the mentioned system. Our derivation of the system reconstruction matrix R assumed that the the sine dependence in eq. 2.2, 2.3 and 2.4 can be neglected. This is a good approximation only when the phase difference is small. However the mirror alignment procedure used in PYPS is an iterative procedure. So initial errors due to the linear estimation of the signals produced by the interaction/reconstruction matrices approach are recovered in the iterative process. We call this process the *closed-loop operation*, that means iterating the measurement and correction steps where the applied command vector $\mathbf{C}$ at step k is:

$$\mathbf{C}(k) = g \cdot R[\mathbf{S}(k) - \mathbf{S_0}] + \mathbf{C}(k-1) \tag{2.9}$$

where $\mathbf{S_0}$ is the so called *slope-null vector* and g is the loop *gain*. $\mathbf{S_0}$ is the signal vector generated when the mirror is in the configuration that the loop have to recover.

2.3 Phase ambiguity solutions

The closed loop correction of the differential piston error is a powerful technique in order to achieve the minimal residual error. On the other hand, as stated in sect. 2.2.1, the closed-loop operation is based on the assumption of the signal linearity. Equations 2.2, 2.3 and 2.4 clearly show the sine dependence of the PYPS signal on the phase difference $\Delta\phi = 2\pi(2\delta)/\lambda$ introduced by a single segment with a physical phase error δ at the working wavelength λ. So we can consider the linearity condition respected when $|\Delta\phi| \ll \pi/2$. When $|\Delta\phi| \leq \pi/2$ the sine function can still be inverted and the piston error retrieved, while in the case $|\Delta\phi| > \pi/2$ the sine introduce an ambiguity that can not be solved in a single measurement. However let's observe the behavior of the closed-loop operation when the piston error is in the range $\pi/2 < \Delta\phi < \pi$. Fig. 2.7 shows schematically the case of a starting differential piston of $\pi/2 < \Delta\phi_{R0} < \pi$ radians. The reconstruction process (sect. 2.2.3) assumes a linear system, so[4] the measured signal (S), generated by the real phase error $\Delta\phi_{R0}$, is associated by the reconstructor to the estimated value $\Delta\phi_{E0}$. Then the correction applied by the closed loop is $\Delta\phi_{E0}$ and in the next loop step we found the residual piston $\Delta\phi_{R1} = \Delta\phi_{R0} - \Delta\phi_{E0}$. Again we are out of the sine inversion range, so the estimated piston error is $\Delta\phi_{E1}$ and the correction once more is underestimated. In the considered case, at

[4]Lets neglect here the non-linearity of the sine function in its inversion range, this does not change the logic of the described process.

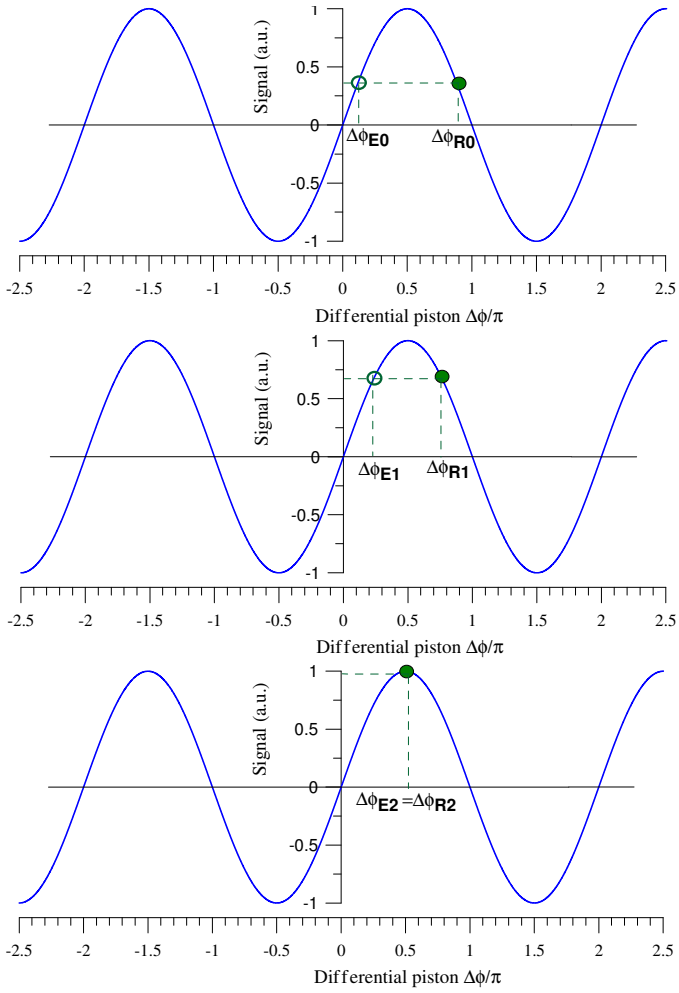

Figure 2.7: These schemes show the behavior of a piston correction closed loop when the initial phase error is in the range $\pi/2; \pi$. The real differential piston $\Delta\phi_R$ is underestimated by the $R\mathbf{S}$ product and the correction is done for the estimated value $\Delta\phi_R$. Anyway, because the correction is done in the good direction, the iterative process (top to bottom) is able to drive the differential piston in the sine inversion region, where the loop is properly working.

the third loop step, the piston error is driven in to the sine inversion range and $\Delta\phi_{R2} = \Delta\phi_{E2}$, so the loop can retrieve the correct zero. This happens while $|\Delta\phi| < \pi$. Let's consider now $\pi/2 < |\Delta\phi| < \pi$ as the case represented in fig. 2.8. Now $\Delta\phi_{R0}$ and $= \Delta\phi_{E0}$ have opposite signs, so the correction applied by the loop is in the wrong direction driving the differential piston to the next stable zero, that in our case is 2π radians.

We obtain the same behavior considering negative $\Delta\phi_{R0}$, so we can say that the closed-loop effective capture range is $[-\pi; \pi]$ in wavefront radians that translates in $\pm 200\, nm$ in physical mirror step while working with a $800\, nm$ wavelength.

The found closed-loop capture range does not cover the one required for the ELT's operations of segment integration (sect. **??**) and realignment after a period of inactivity of the phasing control loop. Two different phasing techniques [36] [37] have been elaborated at Keck telescopes to achieve a larger capture range. Here below we will describe three techniques elaborated to increase the PYPS capture range. The concepts of all techniques has been proved experimentally as reported in the following chapters.

2.3.1 The Multi-Wavelength technique

This phase ambiguity solution technique has been proposed in 2001 by Esposito [25], in this section we will expose the concept more widely. This technique is the one chosen for PYPS in the APE project and has been tested for the first time in 2006 [38] and then consolidated in the PYPS acceptance test (sect. 3.2.4).

This technique is based on the iteration of two steps: a closed loop correction operated at the wavelength λ_{CL} and an open loop measurement at $\lambda_{OL} = \lambda_{CL} + \Delta\lambda$. After a first closed loop run at the wavelength λ_{CL},

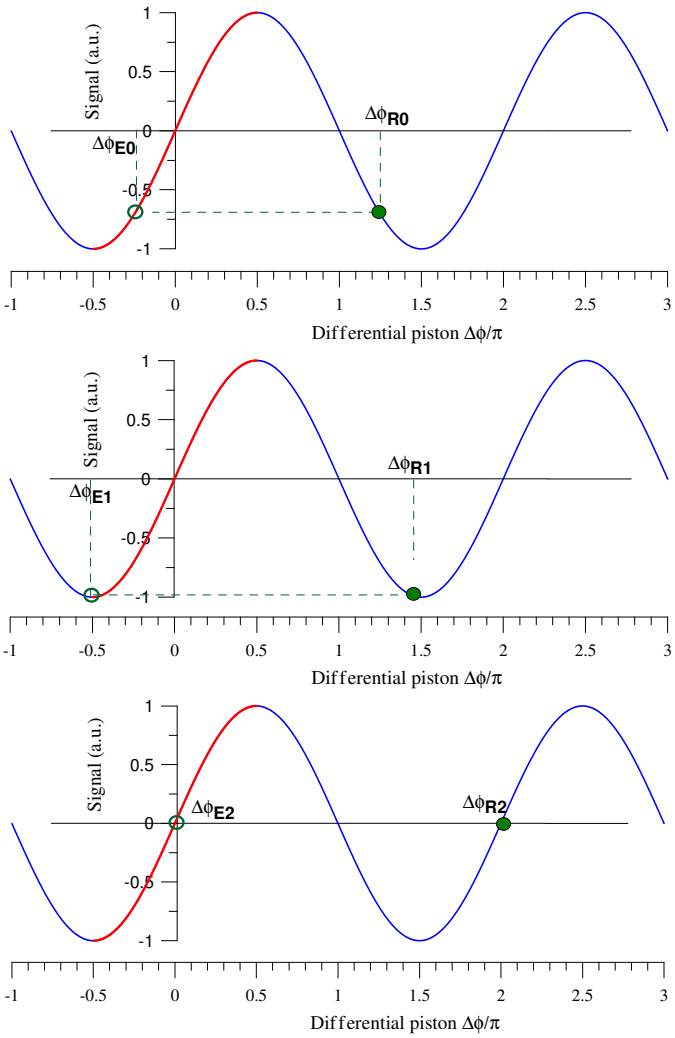

Figure 2.8: The same schemes as in fig. 2.7, but here the initial differential piston is bigger than π. Now the iterative process is applying a correction of sign opposite to the required one. So the closed loop drives the differential piston to the next zero of the sine function with positive slope (stable position for the control loop). This behavior is used in the multi-wavelength technique described in sect. 2.3.1.

all the segment differential pistons ideally reach the value $\Delta\phi(i) = 2k(i)\pi = 2\pi\,[2\delta(i)]/\lambda_{CL}$, where $\delta(i)$ is the physical differential piston on the mirror surface and i is the segment index. Then the operating wavelength is switched to $\lambda_{OL} = \lambda_{CL} + \Delta\lambda$ and a single open loop measurement is done. The physical differential pistons are still $\delta(i) = k(i)\,\lambda_{CL}/2$, so that the signal detected with λ_{OL}, on a sub-aperture on the segment edge, is:

$$S^M_{OL}(i) = C + A\,\sin\left[2\pi\,\frac{2\delta(i)}{\lambda_{OL}}\right] = C + A\,\sin\left[2\pi\,k(i)\,\frac{\lambda_{CL}}{\lambda_{CL}+\Delta\lambda}\right]; \quad (2.10)$$

C is an additive constant due to statical aberration and can be removed subtracting $S^R_{OL}(i)$ the signal of the same sub-aperture measured when $\delta(i) = 0$. Choosing λ_{OL} so that $\Delta\lambda > 0$ and $\Delta\lambda/\lambda_{CL} \ll 1$, the sign of

$$S_{OL}(i) = S^M_{OL}(i) - S^R_{OL}(i) = A\,\sin\left[2\pi\,k(i)\,\frac{\lambda_{CL}}{\lambda_{CL}+\Delta\lambda}\right] \quad (2.11)$$

is opposite to the sign of $k(i)$ as shown if fig. 2.9. That is because $\lambda_{CL}/[\lambda_{CL}+\Delta\lambda] = 1/[1+(\Delta\lambda/\lambda_{CL})]$ is always positive and $\ll 1$, while $k(i)$ is integer by definition. This relationship remains true while the phase difference between S_{OL} and S_{CL} is less then π: $[2\pi\,2\delta/\lambda_{OL}] - [2\pi\,2\delta/\lambda_{CL}] < \pi$. Taking in to account that $k(i) = 2\delta(i)/\lambda_{CL}$ and $\Delta\lambda = \lambda_{OL} - \lambda_{OL}$ we found:

$$k(i) < \frac{\lambda_{OL}}{2\Delta\lambda} \quad (2.12)$$

Once the sign of $S_{OL}(i)$ is known, $\Delta\phi(i)$ can be corrected of $\pm\lambda_{CL}$, according to the measured sign. The procedure closed loop, open loop measurement and piston correction is then iterated until $S_{OL}(i)$ is null for all the segments. The capture range of this technique is found directly from eq. (2.12) obtaining:

$$\delta(i) = \pm\frac{\lambda_{CL}\lambda_{OL}}{4\Delta\lambda} \quad (2.13)$$

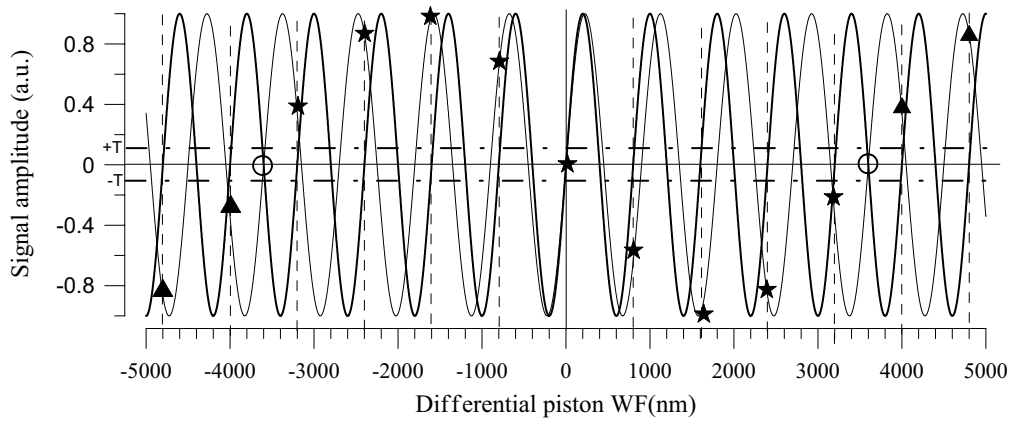

Figure 2.9: In the graph is represented the PYPS signal of a sub-aperture corresponding to a segment edge as function of the wavefront step. The bold and the thin lines represent the signals at $\lambda_{CL} = 800nm$ and $\lambda_{OL} = 900nm$ respectively. The stars and the triangles represent the signal values at λ_{OL}, when the edge step is $\delta = k\,\pi/\lambda$, with k integer. The sign of this signal reveals if the phase ambiguity is on the positive or negative side of the physical step zero. This is true while the phase difference between the two signals is in the range $[-\pi; +\pi]$ (circles in the graph); when this range is exceeded the signal sings are inverted and the λ correction is done in the wrong direction. The values $\pm T$ (points and dashed lines) represent the threshold that can be used to determinate the success of the closed loop operation and the minimum amplitude of the open loop measurement to detect the phase ambiguity. In this example the value of T corresponds to a physical step of $\sim 20\,nm$ that is larger than the expected accuracy achieved by the closed loop operation.

Typical wavelengths in this application are $\lambda_{CL} = 850nm$ and $\lambda_{OL} = 900nm$; for these values we find a capture range $\delta = \pm 3.8\mu m$.

The main advantages offered by this technique are the parallel correction, so that the operational time is not dependent on the number of segments, and the accuracy reached, that is the same of the single wavelength closed loop. The main limitations are the finite capture range, that is basically dependent on the single closed loop accuracy, and the need of calibration data like the interaction matrix and the slope-null vector. The last limitation prevents the use of the technique for the mirror first phasing.

2.3.2 Segment sweep

This technique is based on the phase step signal behavior when the reference source has a finite bandwidth source, as used by Chanan et al. at Keck telescopes [36] [37]. In sect.2.1.1 we demonstrated (eq. 2.5) that the signal dependence on the physical step δ becomes:

$$S \propto 2\delta \Big[Ci[t] - \frac{\sin[t]}{t} \Big]_{4\pi\delta/\lambda_2}^{4\pi\delta/\lambda_1} \tag{2.14}$$

where λ_1 and λ_2 are the two extremes of the used wavelength bandwidth and Ci is the *Cosintegral* function. The working principle of the technique is to solve the phase ambiguity thanks to this signal amplitude modulation. Fig. 2.10 represents the amplitude modulation in the case of $300\,nm$ bandwidth. In this case the amplitude modulation of the maxima and minima clearly identify the zero correspondent to $\delta = 0$. This, in practice, will happen when the signal amplitude depression between two consecutive maxima is larger than the signal indetermination. This phase ambiguity solution can be used to phase the mirror segments taking one segment as reference and sweeping the neighbors. Recording the signal, at each sweep step, on the edge between

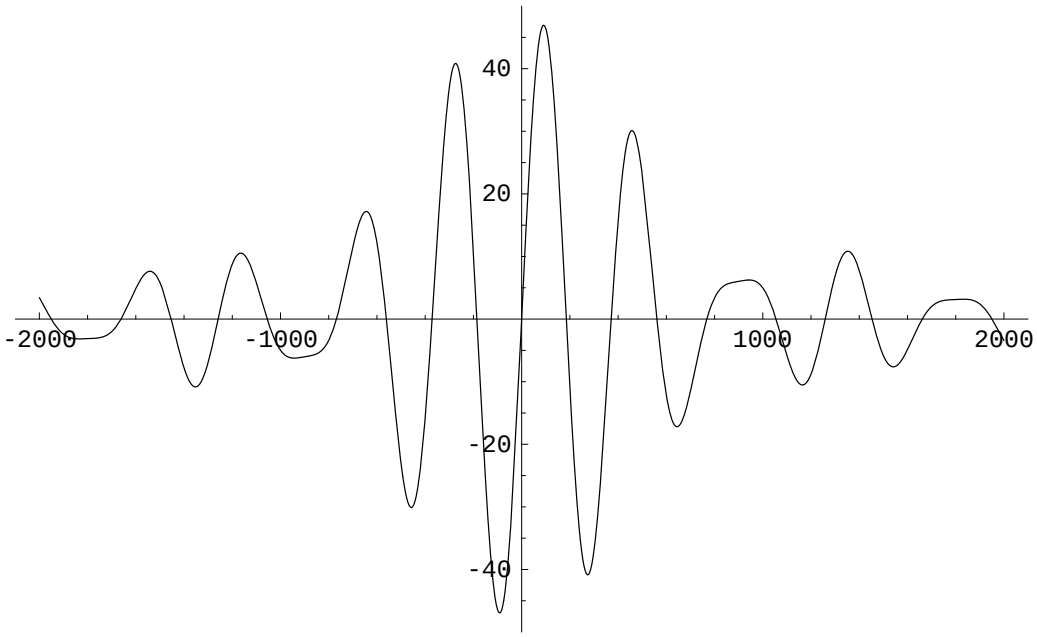

Figure 2.10: The theoretical broadband PYPS signal (eq. 2.5) in arbitrary units as function of the mirror step reported in nm. The considered λ_1 and λ_2 are respectively 600 and $900nm$ as the source used for the first flattening of the segmented mirror at the William Herschell Telescope (sect. 4.2). This plot can be compared with the one obtained experimentally and reported in fig.4.5.

the reference and sweeping segments, the maximum and minimum around $\delta = 0$ can be identified. Then the mean position between these two values is the best estimation of the zero differential piston.

So, this technique allows removing the phase ambiguity and finding the phased position without the need of any sort of pre-calibration as required by the closed-loop techniques that require a phased position in order to acquire the interaction matrix and the reference signal vector (sect. 2.2.3). It is easy to understand that the capture range of the SST is theoretically infinite, but large ranges are payed in terms of time. The operational time is the main

limit of this technique because the sweeping procedure can be only partially parallelized, so there still remains a dependence of the phasing time on the segment number. We can give an order of magnitude of the required time considering a capture range of $\pm 20\,\mu m$ on the mirror surface and a segment settling time of $0.5\,s$. For the hexagonal segment geometry, as chosen for TMT and E-ELT, the sweep has to be performed ring by ring. Knowing that the relation between the number of segment N and the number of rings N_R is $N = 3N_R(N_R + 1)$, for $N \sim 900$ we got $N_R = 17$. To properly recognize the zero that identify $\delta = 0$, we require at least 10 measurement per equivalent wavelength. Taking this quantity as $\lambda = 800\,nm$, we obtain 100 wavelengths in the range and so 1000 steps for each sweep. So the are $500\,s$ for each ring and more than 2 hours of effective measurement time for the whole mirror phasing. Moreover, if the wavefront sensor is working in seeing limited conditions, we need to average out the atmospheric disturbance. In this case the single step time is dominated by the several seconds of exposition required by the turbulence averaging and the total phasing time results of tens of hours. Another limit is that the accuracy relies also on the repeatability of the segment piston commands, that is because every segment has to be swept passing through the phased position and then repositioned after the signal analysis.

Despite these important limitations the SST is the only technique (in the three proposed in this chapter) able to provide a *first phasing* where the interaction matrix has been successfully acquired. That is the important role played by this technique during the experimental runs at the William Herschel Telescope (see chapter 4).

2.3.3 Wavelength sweep

The Wavelength Sweep Technique (WST) is based on the piston signal dependence on the wavelength λ. Remembering that $\Delta\phi = 2\pi(2\delta)/\lambda$, the sine dependence on the phase step $\Delta\phi$ (see sect.2.1) translates in a sine dependence on $1/\lambda$. The period of this sine is simply 2δ; then measuring the signal for several values of λ we can fit $S(1/\lambda)$ with the function $S_f(1/\lambda) = C_f + A_f \sin[2\pi\, T_f(1/\lambda) + P_f]$, obtaining C_f, A_f, T_f, P_f, with $T_f = 2\delta$. This measurement gives an estimation of the physical step that lies on the considered sensor sub-aperture. Supposing the segment tip&tilt error negligible, this is a differential piston measurement.

The working limits of this technique are the minimum and the maximum detectable step. The minimum physical step δ_m that can be measured using the WST is defined by the extreme values of the wavelength λ_s and λ_e applicable in the sweep. That is because, in order to fit the period of the sine function, a minimum phase variation $\Delta\phi_m$ is required. Sweeping from λ_s to λ_e, we obtain $\Delta\phi = 2\pi\, 2\delta\, (\lambda_e - \lambda_s)/(\lambda_e\, \lambda_s)$ and δ_m is defined as the minimum step that induces the phase variation $\Delta\phi_m$:

$$\delta_m = \frac{\Delta\phi_m}{4\pi} \frac{\lambda_e\, \lambda_s}{\lambda_e - \lambda_s}. \tag{2.15}$$

In order to ensure a proper fitting of the sine period, we can require $\Delta\phi_m = \pi$, obtaining $\delta_m = \lambda_e\, \lambda_s \,/\, 4(\lambda_e - \lambda_s)$.

The other WST limit is the maximum detectable step δ_M. This value is defined by the finest wavelength variation $\Delta\lambda_m = \lambda_{i+1} - \lambda_i$ applicable between two consecutive sweep steps. In order to properly fit the period of the sine function, we have to impose a maximum phase variation $\Delta\phi_M$ due

to the wavelength variation $\Delta\lambda_m$. Then we find:

$$\delta_M = \frac{\Delta\phi_M}{4\pi}\frac{\lambda_{i+1}\lambda_i}{\Delta\lambda_m}. \tag{2.16}$$

Being conservative we can double the theoretical value of maximum phase step choosing $\Delta\phi_M = \pi/2$, obtaining so $\delta_M = \lambda_{i+1}\lambda_i/(8\Delta\lambda_m)$.

The generic step δ can be seen by PYPS as positive or negative according to the sensor signal definition. Fitting the signal $S(1/\lambda)$ with the function $S_f(x) = C_f + A_f \sin[2\pi\, T_f x + P_f]$, the sign of T_f is supposed to be positive, so $\delta = T_f/2$ is supposed positive too, and the information on sign of δ is lost. Practically we can better say that $T_f = 2|\delta|$. So, in presence of $\Delta\phi < 0$, we have: $\sin\left[\Delta\phi\right] = \sin\left[-2\pi\, 2|\delta|/\lambda\right] = \sin\left[\pi + 2\pi\, 2|\delta|/\lambda\right] = -\sin\left[2\pi\, 2|\delta|/\lambda\right]$. Therefore the sign of δ is determinable through the value of P_f (0 or π) considered together with the sign of A_f.

The WST becomes interesting considering the commercial availability of devices as the Liquid Crystal Tunable Filters (LCTF). These instruments allows to select the working bandwidth with a $\Delta\lambda_m < 1\,nm$ in ranges wider than $300\,nm$. Lets consider as example the model SNIR-10-20-STD produced by Lot Oriel Group. This device has a working range $[650\,nm; 1100\,nm]$ with a bandwidth of $10\,nm$. Taking in to account also the quantum efficiency of the CCD detector used in PYPS, we can estimate the WST limits considering $\lambda_s = 650\,nm; \lambda_e = 950\,nm; \Delta\lambda_m = 1\,nm$. Introducing these values in eq.2.15 and 2.16 we found:

$$\begin{aligned} \delta_m &\sim 500\,nm \\ \delta_M &\sim 100\,\mu m \end{aligned} \tag{2.17}$$

Using the considered LCTF the maximum detectable step we found that is no more limited by δ_M, but by the coherence length (as represented in fig. 2.3)

given by the $10\,nm$ bandwidth centered at $800\,nm$, that is $64\,\mu m$ corresponding to $32\,\mu m$ on the mirror surface. This limitation can be solved, introducing in the optical path a second LCTF driven with a shifted wavelength respect to the first one. Therefore, we can obtain a narrower bandwidth, paying, of course, in term of transmission, but extending the capture range.

The working principle of the WST has been validate with some preliminary measurement performed with PYPS during the test period in the Arcetri labs. The test results are reported in sect. 3.2.5.

Similar results, in terms of capture range ($\pm 30\,\mu m$), were achieved in 1998 at Keck telescopes [36]. The used technique requires the segment sweeping, that does not represent a big limitation for a 36 segments, but represents a killing factor when applied to ELTs with hundreds of elements. So, the main advantage afforded by the WST is the simultaneous estimation of all the mirror steps with a single wavelength sweep, measurement that does not require any segment movement. Having the signal values at all the sweep steps, the mean piston error of each segment can be estimated with an off-line algorithm and the mirror phased. It is important to note that no system calibration is required for this technique, as opposite to all the closed loop techniques where an interaction matrix and a reference position acquisitions are required.

Chapter 3

Pyramid Phasing Sensor for APE

In this chapter we describe the work done and the results obtained up to now with the PYPS developed and realized for the APE experiment (see sect. 1.3). The wavefront sensor design and concept passed the APE **critical design review** at ESO in December 2005. After this milestone, the optical design has been reviewed, reaching the final version described in the following section. The procurement and assembling phase has been accomplished at the end of 2006, followed by a test phase in the first months of 2007 and closed by the PYPS system **acceptance test** done in April 2007 at the Arcetri premises as shown in sect. 3.2.

3.1 PYPS optical design

The PYPS optical design has been derived from the one of the WFS of the LBT First Light AO system developed by the AO Arcetri group [39]. The main difference between the two WFSs are the FoV and the pupil sampling.

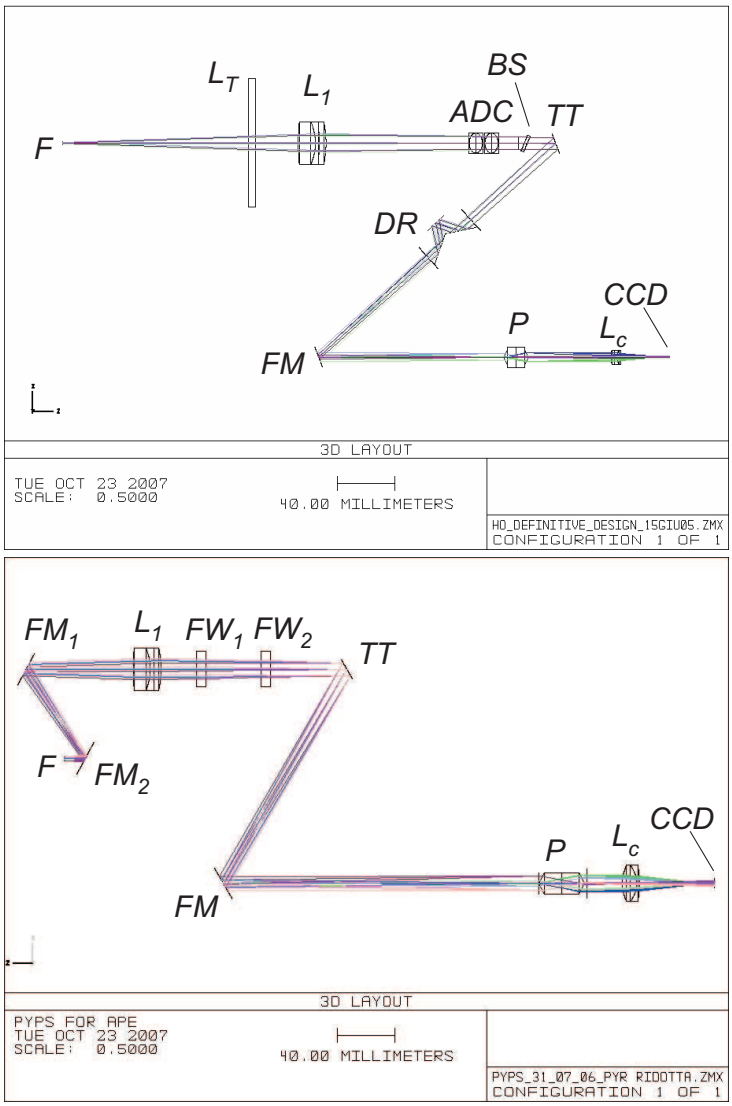

Figure 3.1: The optical designs of PYPS (**bottom**) and of the LBT WFS (**top**). The designs have been realized with *ZEMAX-EE Optical Design Program*. In both cases the source (F) is represented by the focal plane of an f_{15} beam coming from the left side of the schemes. The different ray colors represent different field of view in the range $\pm 1.5''$ and $\pm 3.0''$ for LBT-WFS and PYPS respectively.

In both schemes (fig. 3.1), the main components of the PWFS are present: the input lens (L_1), that focuses the incoming f_{15} telecentric beam in the plane where is located the pyramid (P) vertex and generates a pupil image on top of the fast steering mirror (TT); this device provides the tip&tilt modulation; the camera lens (L_C) creates the four pupil images on top of the CCD detector plane (CCD). Some minor modifications to the general optical layout have been done. The PYPS beam has been folded with the plane mirrors FM_1 and FM_2 in order to match the opto-mechanical constrains on the APE main bench. Two filter wheels (FW_1 and FW_2) have been added in the optical path allowing to introduce colored filters for the multi-wavelength technique (see sect.2.3.1). Some elements have been removed because their

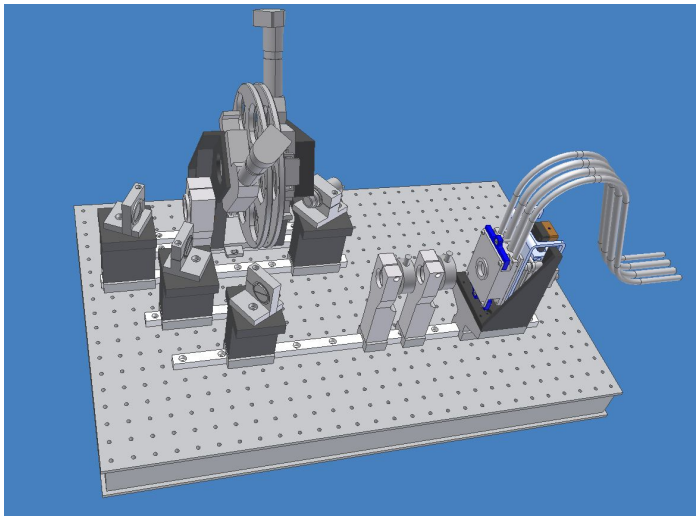

Figure 3.2: 3D view of the PYPS mechanical layout.

functionalities are embedded in the APE main bench. The removed elements are: the atmospheric dispersion corrector (ADC), the pupil de-rotator (DR), the beam-splitter (BS) and the telecentric lens (TL). All the optics have been arranged in custom mechanical mounts developed in collaboration with

the company *ADS International*. An overall view of the finalized mechanical design of PYPS is shown in fig. 3.2.

3.1.1 PYPS field of view

We said that the required FoVs are different, that is because the LBT sensor, as AO WFS, is optimized to work in diffraction-limited regime. Indeed the diffraction limited PSF of an $8.4\,m$ pupil at $600nm$ presents a $FWHM = \lambda/D \sim 15\,mas$, so the LBT WFS has a FoV of ± 1.5" containing all the PSF structures. On the contrary APE will be operated in seeing-limited conditions. Therefore, in the optical design the PYPS FoV has been enlarged up to ± 3" to avoid loss of information in the typical condition of a seeing disk of 1.0". The FoV enlargement has mainly required the modification of the pyramid and the camera lens. The diameter of the pyramid have been linearly scaled with the enhancement of FoV, because the pyramid lies on the focal plane (and both WFSs are working with an f_{45} beam on the pyramid). Hence, the pyramid diameter has been modified from $10\,mm$ to $15\,mm$[1]. Let's now note that, as for the LBT AO WFS, the PYPS pyramid is composed by two glass pyramids. The optical design of the double pyramid of both WFSs is reported in fig.3.3. All the details about the LBT WFS pyramid design are reported in [40], here we just remind that: the beam angle separation obtained by a double pyramid is very close to the one obtained by a single pyramid with vertex angle equal to the difference of the two composing the double pyramid. The fundamental advantages with the double pyramid respect to the single one are the chromatic correction, obtained using different glasses for the two elements, and the wider vertex angle of the pyramids, that allows to obtain sharper edges in the glass polishing process.

[1] In both cases, the pyramid diameter is not the limiting factor of the WFS FoV.

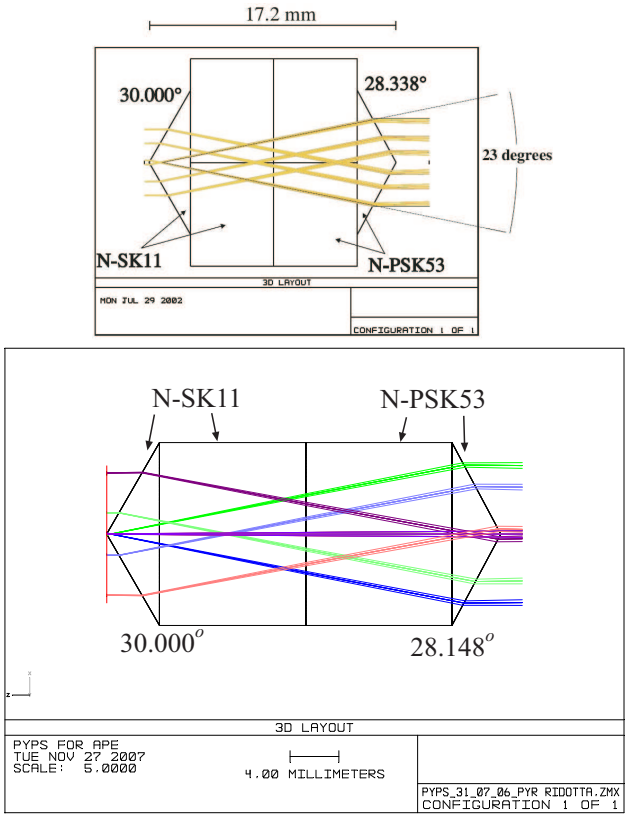

Figure 3.3: The double pyramid optical designs. The one for the LBT AO WFS (**top**) and for PYPS (**bottom**). For both projects the pyramid glasses are N-SK11 and N-PSK53 from the *Schott* catalog.

A single pyramid is a highly dispersive element because each single face acts as a prism; with the used configuration we achieved a good chromatic correction in the range $650 \div 950\,nm$ in the pupil plane. The double pyramid design required another modification to effectively provide a wider FoV. The thickness of the glass between the two pyramid vertices has been increased from $14\,mm$ up to $32.3\,mm$. The reason is evident looking again at the sketches in fig.3.3: after the refraction on a face of the first pyramid, the beam needs the space to cross the optical axis before the refraction on the

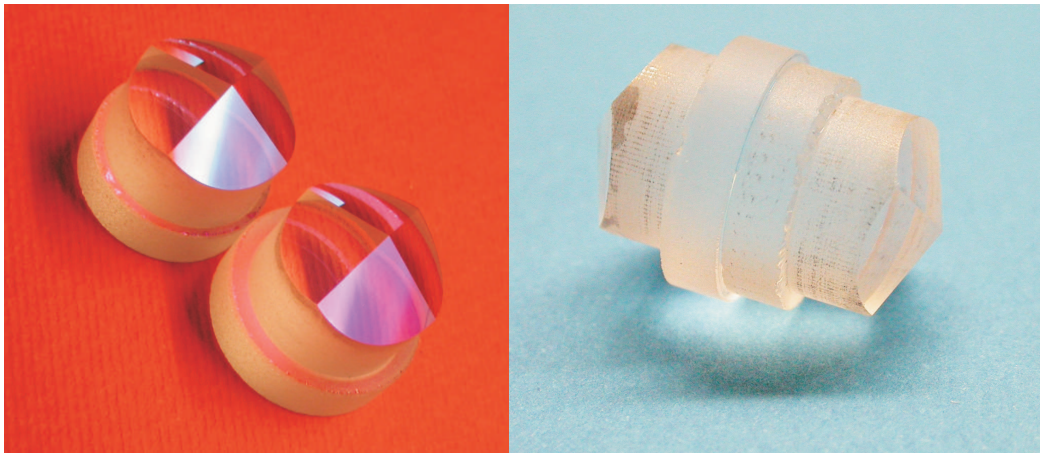

Figure 3.4: The two elements composing the PYPS double pyramid polished at the Arcetri promises, before (**left**) and after (**right**) the final gluing.

correct face of the second pyramid. The more a beam is off-axis, the more optical path is the required between the two pyramid vertices. This, together with the dimension of the second pyramid, result to be the real limiting factor for the sensor FoV.

3.1.2 Pupil sampling

Once the correct FoV is achieved, we have to modify the pupil sampling. As discussed in sect. 1.4, the pupil arrangement on the CCD detector defines the pupil sampling. In sect. 2.2.2 we saw that, with a square segmentation geometry, it is possible to reconstruct piston and tip&tilt with $2X2$ sub-apertures per segment. On the other hand, the hexagonal geometry does not match the square geometry of the CCD pixel grid, so the best sampling can not be found simply through logical deductions. In order to experimentally study the efficiency of different pupil samplings, we choose to sample each segment side-to-side with 12 sub-apertures. This optical arrangement

allows us to choose the sampling between the $12 - 6 - 4 - 3$ sub-apertures, simply selecting the CCD binning to the value $1X1 - 2X2 - 3X3$ and $4X4$ respectively. However, the foreseen operative samplings are only with 6, 4 and 3 sub-apertures per segment, while the one with 12 will be useful for the alignment operations. From the optical design point of view, the pupil

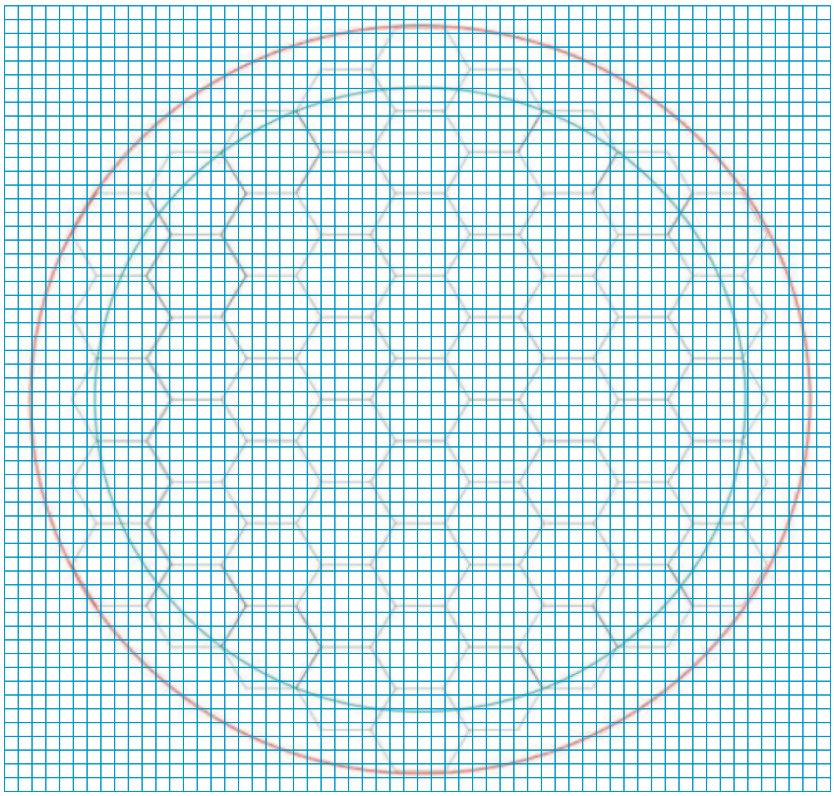

Figure 3.5: A sketch representing the sub-aperture grid with respect to the pupil (green circle) and the ASM segment geometry (black hexagons). The case illustrated is the one with 6 sub-apertures per segment side-to-side, obtained when the CCD is binned by $2X2$. The shown arrangement allows to place all the horizontal segment edges across a sub-aperture obtaining the maximum signal efficiency.

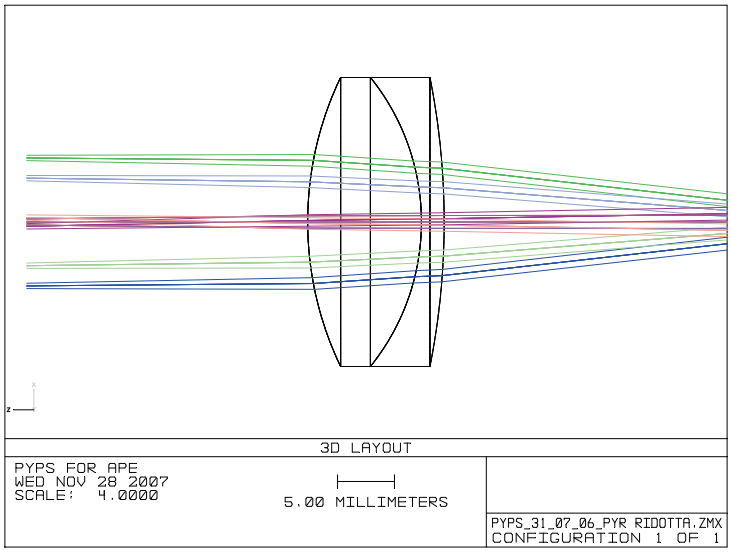

Figure 3.6: The custom design of the PYPS camera lens. This element is an achromatic doublet, the biconvex part is in FK51 glass, while the meniscus is in F2.

images size and separation are defined by the focal lengths of L_1 and L_c plus the effective angle of the pyramid. L_1 creates a pupil image (the pupil comes from infinity because the incoming beam is telecentric) on the fast steering mirror TT surface that is imaged on the CCD plane by L_c. So, the real size of the pupil images is defined by the ratio of the L_1 and L_C focal lengths, while the separation in between the four images by the pyramid angle and the working $f_{\#}$. The ASM (the APE segmented mirror, see sect. 1.3) has segments of $17\,mm$ side-to-side and the system pupil is imaged on its surface with a diameter of $130\,mm$. So, there are 7.6 segments across the pupil and we need 90.8 pixels on each pupil image to have the chosen ratio of 12 pixels per segment side-to-side. Once the correct pupil arrangement on the CCD surface (the camera is provided by ESO, while the chip is a CCD57-10 aimo produced by *E2V*) is defined, we chose to keep fixed the L_1 design modify-

ing L_C (the lens design is reported in fig.3.6), in order to achieve the correct magnification.

The separation between the pupils has been defined in 41.2 pixels. This number fix the separation between the centers of two adjacent pupils in $90.8 + 41.2 = 132.0$ pixels. This number is a multiple of $2; 3; 4$, so when the CCD is binned by these integers, the sampling is the same on all the four pupils. In order to achieve this separation, the second pyramid angle has been slightly changed from 28.338^o to 28.148^o. The pupil arrangement on the CCD frame is resumed in fig. 3.7.

3.2 PYPS acceptance test

The PYPS acceptance test took place successfully in April 17th-20th 2007 at the Osservatorio di Arcetri, under the supervision of ESO personnel responsible for the APE project. The main goal of these tests was to demonstrate the full functionality of the PYPS system as far as it was allowed by the test tools available in the Arcetri laboratories.

3.2.1 Test setup

A dedicated optical setup was designed and aligned to perform the PYPS acceptance test. A schematic of the optical setup is shown in fig. 3.9. The main components of the setup are:

1. **PYPS board**. The PYPS board hosted all the definitive optical and mechanical components except for the final double pyramid which was still in the polishing phase during these tests. Therefore, all tests were performed with the testing double pyramid of the LBT first-light AO wave-front sensor.

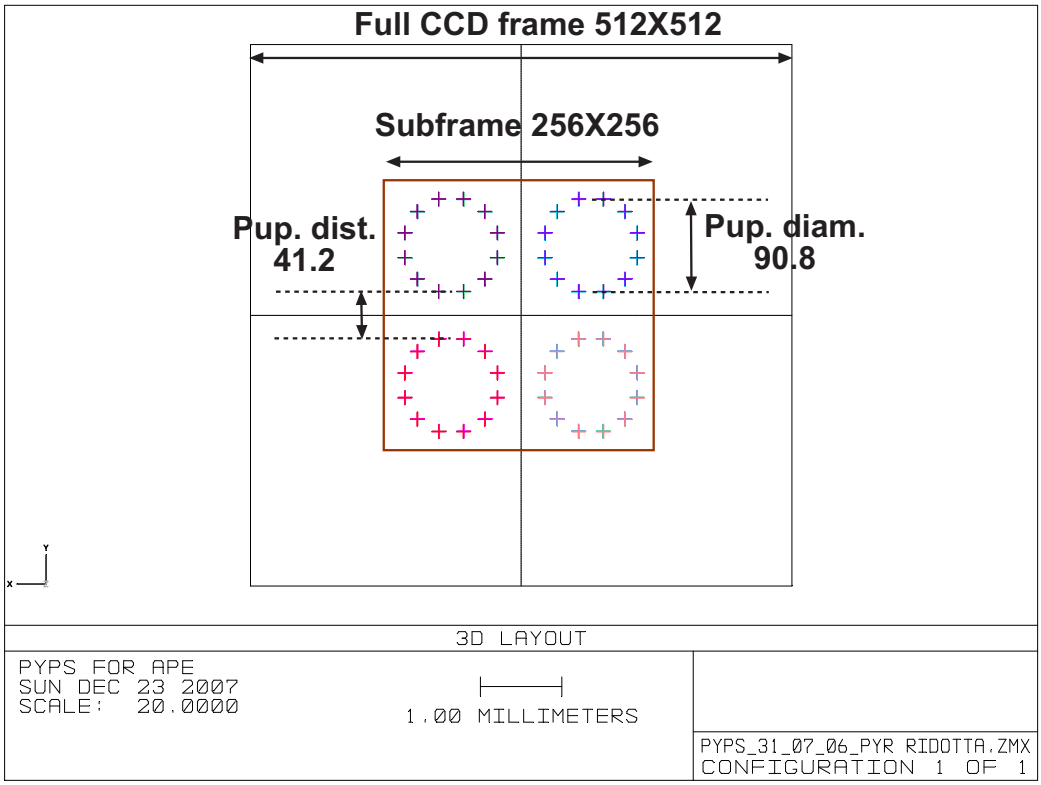

Figure 3.7: The four pupil as arranged on the CCD frame by the optical design. Only a sub-frame of $256X256$ will be used of the $512X512$ available. The pupil diameter and distance are expressed in pixels of $13\,\mu m$ side.

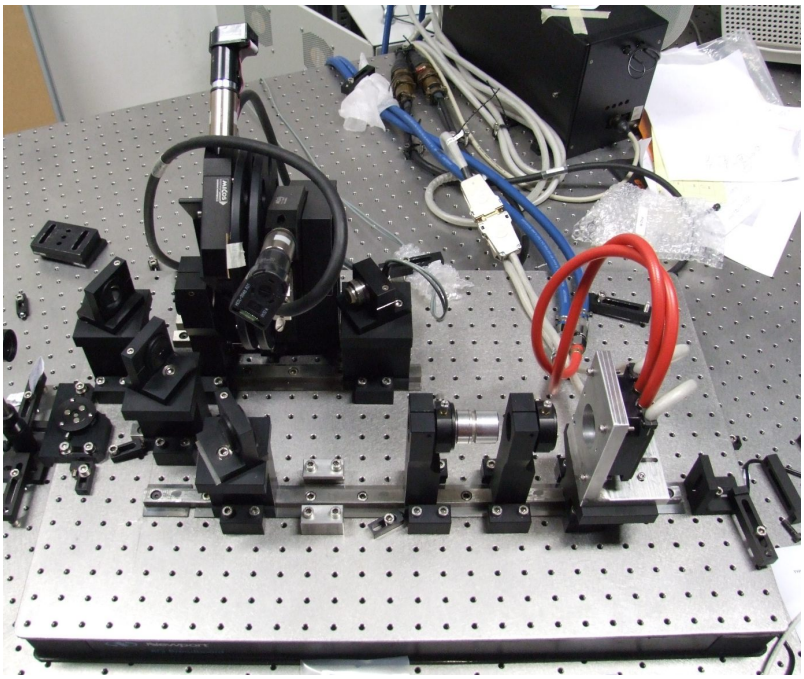

Figure 3.8: PYPS assembled and aligned in the Arcetri lab, ready to perform the acceptance test.

2. **Deformable mirror**. PYPS was coupled with a commercial segmented MEMS (Boston Micromachines SLM140) having 12x12 square segments with 300 μm inter-actuator pitch. Each segment can be displaced in piston with a 10 nm resolution on the mirror surface (i.e. 20 nm on the wavefront). The MEMS was conjugated to the system pupil. Between 9 and 10 segments were present across the pupil diameter, each segment side being sampled by 10 sub-apertures.

3. **Light source**. The system has been illuminated with a non resolved fiber, feeded by a commercial halogen lamp.

4. **Turbulence generator**. A reflecting phase screen (SINFONI test phase screen on loan from ESO) was introduced to emulate a single-layer atmosphere with a seeing of 0.6″ for an 8 m pupil. The rotating

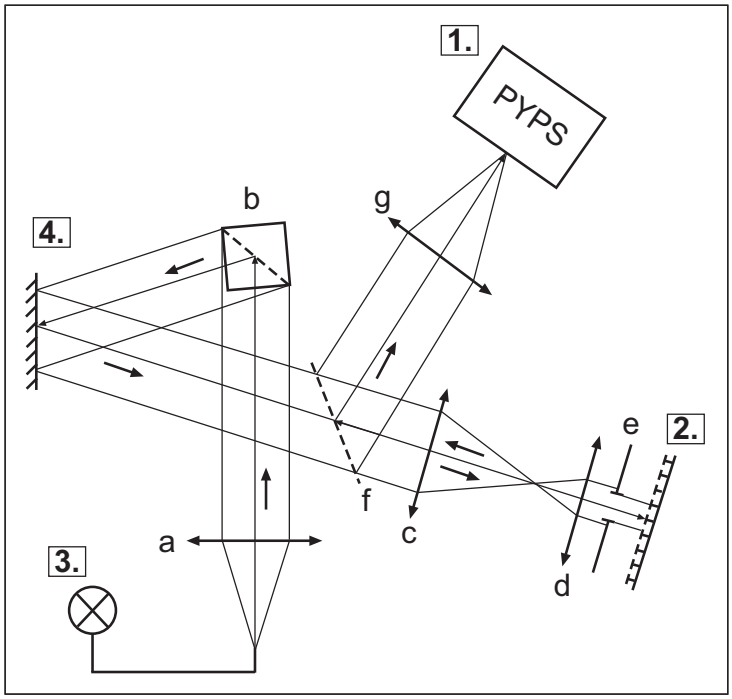

Figure 3.9: A sketch of the laboratory setup arranged to perform the PYPS acceptance test. All the parts are described in the text and the real system is represented in fig.3.10

speed of the phase screen was set up to emulate an equivalent wind speed of 15 m/s.

The reference source (3.) is a fiber feeded by a halogen lamp positioned in the focus of a collimating lens (a). The beam, steered by a cube beam-splitter (b), is reflected by the phase-screen (4). Then the beam is shrunk by an afocal system (composed by the lenses c and d) used to fit the beam on the MEMS (2.) size. The system pupil stop (e) is positioned just in front of the segmented mirror illuminating $9 \div 10$ segments in the pupil diameter. Afterwards the light passes back through the afocal system, folded by a pellicle beam-splitter (f) and focalized by the lens (g.). The pupil stop is

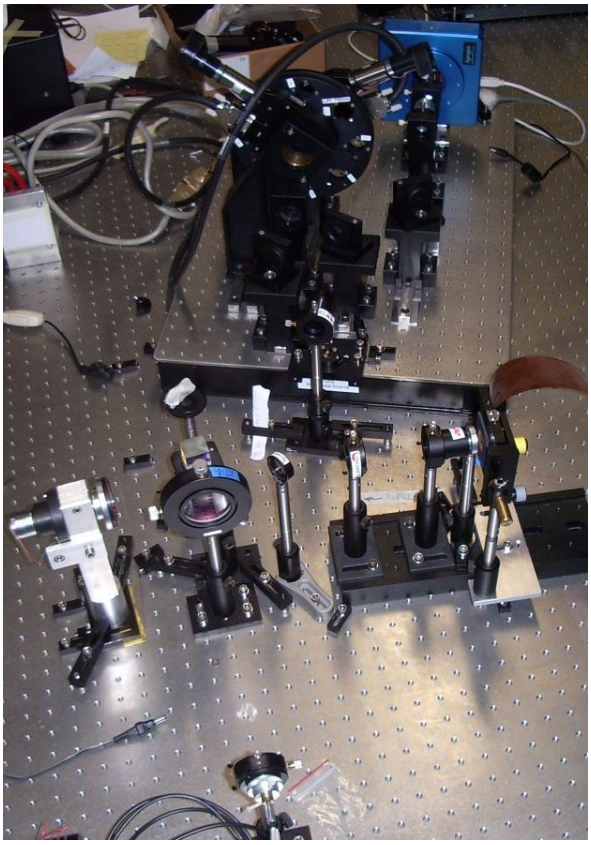

Figure 3.10: The optical system realized for the acceptance test of PYPS (on the top of the picture) at the Arcetri labs. An optical sketch of this setup is reported in fig. 3.9

imaged by the afocal system on the phase screen and on the focal plane of the lens (g.), so that the turbulence is introduced in the pupil plane and the f_{15} beam generated by (g.) results telecentric. This system reproduces the optical condition on the APE main bench, with the limitations of a single turbulence layer (instead of the three available on turbulence generator of APE called MAPS) and the several differences between the MEMS and the ASM.

3.2.2 Calibration

We define PYPS calibration the ensemble of the operations required in between the finalized optical alignment and the closed-loop correction. We describe in this section the principal calibration tasks: the *pupil acquisition*, the *interaction matrix* and *slope-null vector* measurements.

Pupil acquisition

The goal of the pupil acquisition is determine the values of the center and the radius of each of the four pupil images present on the CCD frame. As an example, fig. 3.11 shows a raw frame acquired during the acceptance test and provides some insight on the algorithm developed at Arcetri to perform the pupil acquisition. The first step for the pupil acquisition is based on two threshold values: the first to get rid of the eventual background and the second for the estimation of the pupil area. Of course, the algorithm is more complex, but we don't want to go deeper in details. The tip&tilt modulation is usually increased during the frame acquisition, in order to minimize the spill-out of diffracted light. The second step of the pupil acquisition is the so-called registration refinement. This is an algorithm that fine-tunes the coordinates of the pupil centers determined with the thresholds. This second phase is required to ensure the correct signal computation, that happens when the four pixels (one for each pupil) corresponding to the same subaperture are correctly identified. To perform this optimization, a segment is pistoned on the mirror, then the sensor signals are calculated changing the pupil centers of one or few pixels with respect to the values found in the first estimation. The pupil center values that maximize the signal amplitude are recorded and used for all the following signal computations.

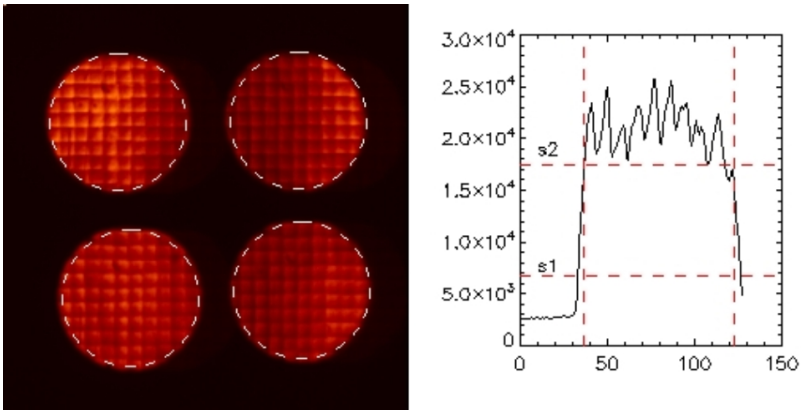

Figure 3.11: **Left:** the raw frame used for the pupil acquisition. The exposure time is $30\,s$, in order to average the turbulence and the modulation is $10\lambda/D$. Higher is modulation, lower is the sensor sensitivity; so that the pupil images are more homogeneous and the pupil acquisition process more efficient. **Right:** a profile across one of the pupil images showing also the two thresholds used in the first step of the centers and radii evaluation. $s1$ defines the background rejection and $s2$ the pupil edge.

Interaction matrix measurement

The interaction matrix between the MEMS and PYPS was acquired using the Interaction Matrix Masking (IMM) technique described in sect. 5.1.1 and [41]. It is important to note that this technique allows performing a parallel interaction matrix acquisition. Therefore, the 4 sets of non-contiguous segments have been defined[2] and for each set the signals have been recorded when the actuators were set $+5$ and -5 MEMS steps. Each mirror step introduces a differential piston of $\sim 20\,nm$ on the wavefront; this value is

[2]During the parallel M acquisition, sets of isolated segments are simultaneously acted; that means segment having no contiguous edges or corners. The square geometry requires 4 sets in order act all the segments, while the hexagonal one only 3.

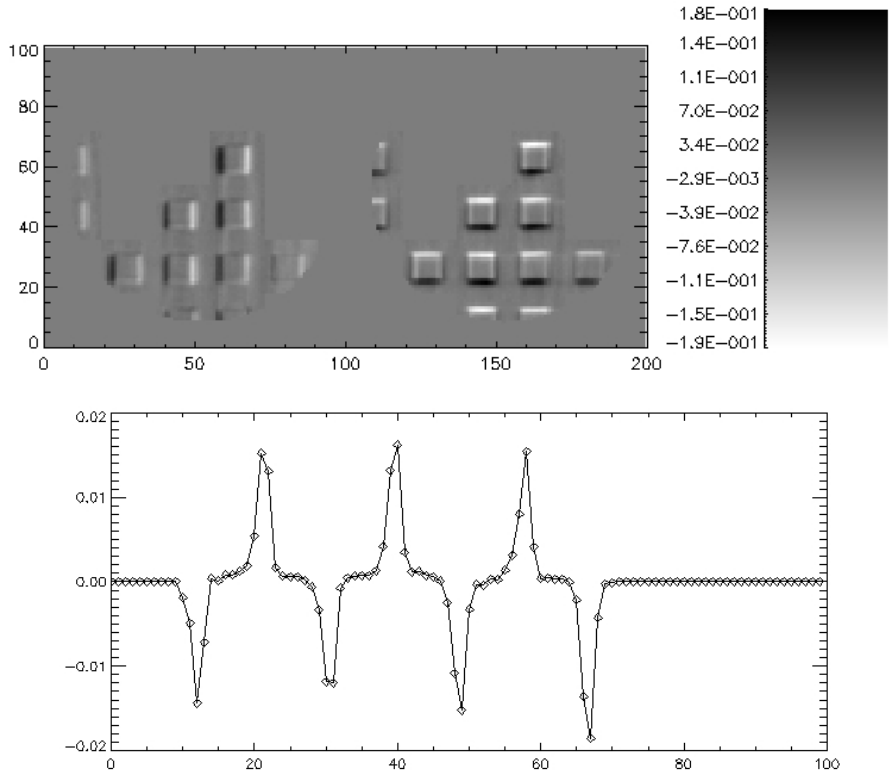

Figure 3.12: **Top:** the signals (S_x left and S_y right) of one of the four segment sets used in the parallel interaction matrix acquisition. **Bottom:** a vertical cut of the S_y signal operated across a segment column. The signal behavior is confirming the simulation results reported in sect. 2.1.1. Let's note the non integer ratio (slightly more than 10) in between sub-aperture and segment size. This is highlighted by the resulting different sampling on consecutive edges.

chosen in order to generate a clear PYPS signal keeping the sine response in the linear range. Fig. 3.12 shows one signal set. The calibrated masks are then used to digitally split the signals and place them in their corresponding columns of the interaction matrix.

Slope-null vector acquisition

Prior to acquiring the slope-null vector the MEMS is set to its reference position by applying the bias signal of 50 steps to all actuators. In order to average out the effects of the atmospheric disturbance 20 CCD frames were acquired and averaged. The slope-null vector is then computed from the final (average) CCD frame. Fig.3.13 shows an example of a slope-null vector acquired during the acceptance test.

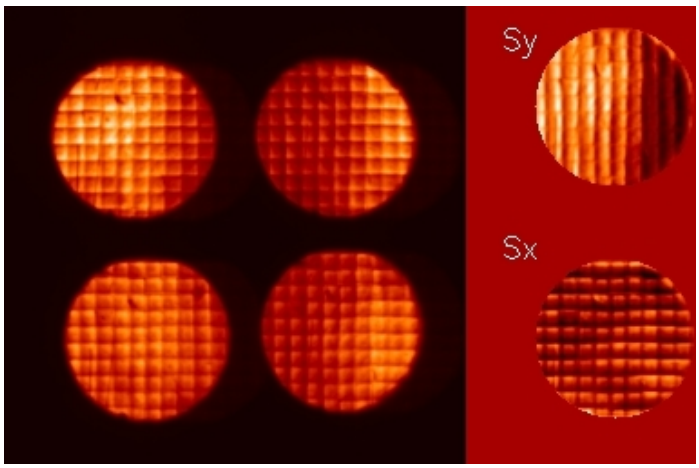

Figure 3.13: Slope-null vector. (**Left**) CCD frame. (**Right**) x- and y-signals..

3.2.3 Closed-loop operation

In this section we will summarize the experimental results obtained during the PYPS acceptance test that demonstrate the closed-loop mono-wavelength mode of operation. The closed-loop has been performed following the theoretical description in sect. 2.2.3. The experimental conditions and main parameters are listed below:

- single layer turbulence with an equivalent seeing of $0.6''$ for a $8\,m$ pupil

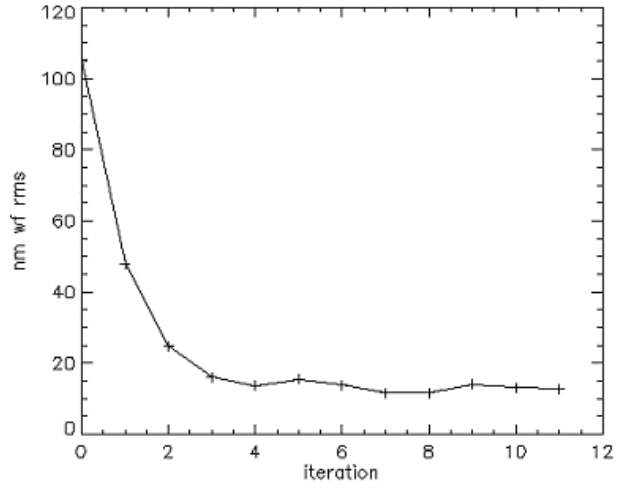

Figure 3.14: Example of phasing closed-loop performed during the acceptance test. For each loop step (horizontal axis) is represented the residual rms (vertical axis) of all the actuators with respect to the reference position.

- 52 selected MEMS actuators were simultaneously controlled
- the initial MEMS position vector was a scrambled vector with a peak-to-valley of $350\,nm$ and $100\,nm$ rms in wavefront [3]
- gain of the integrator -0.7
- tip-tilt modulation $4\lambda/D$
- working wavelength $700\,nm$ with bandwidth $40\,nm$
- the Low-Order Removing (LOR) filtering technique (described in sect. 5.1.2) was applied filtering the first 3 Zernike modes in the PYPS signal space

[3]Note that the initial wave-front piston error for the mono-wavelength tests needs to lie within the capture range discussed in sect. 2.3.

- exposure time: $36\,s$
- binning mode: 1X1 [4]

A typical result is reported in fig.3.14. As can be seen, the loop converges after a few iterations reaching the maximum performance attainable by the MEMS, i.e. the fluctuation of ± 1 actuator step.

3.2.4 Multi-wavelength closed-loop

In this section we will summarize the experimental results obtained during the PYPS acceptance test that demonstrate the multi-wavelength closed-loop, performed following the theoretical description in sect. 2.3.1.

The experimental conditions and parameters were the following:

- color filter used for the closed-loop correction λ_{CL} is $700\,nm$ central wavelength and $40\,nm$ bandwidth
- color filter used for the phase ambiguity solution λ_{OL} is $900\,nm$ central wavelength and $40\,nm$
- 52 selected MEMS actuators were simultaneously controlled
- the initial MEMS position vector was a scrambled vector with a peak-to-valley of $720\,nm$ and $265\,nm$ rms in wavefront[5]
- the multi-wavelength threshold was set to $75\,nm$ (i.e. 3.75 actuator steps).

[4] At the acceptance test, the CCD camera was not able to properly operate the other binning modes.

[5] In order to work within the operational range of the MEMS, the initial position vector was an all-positive vector, as shown in fig. 3.15(top).

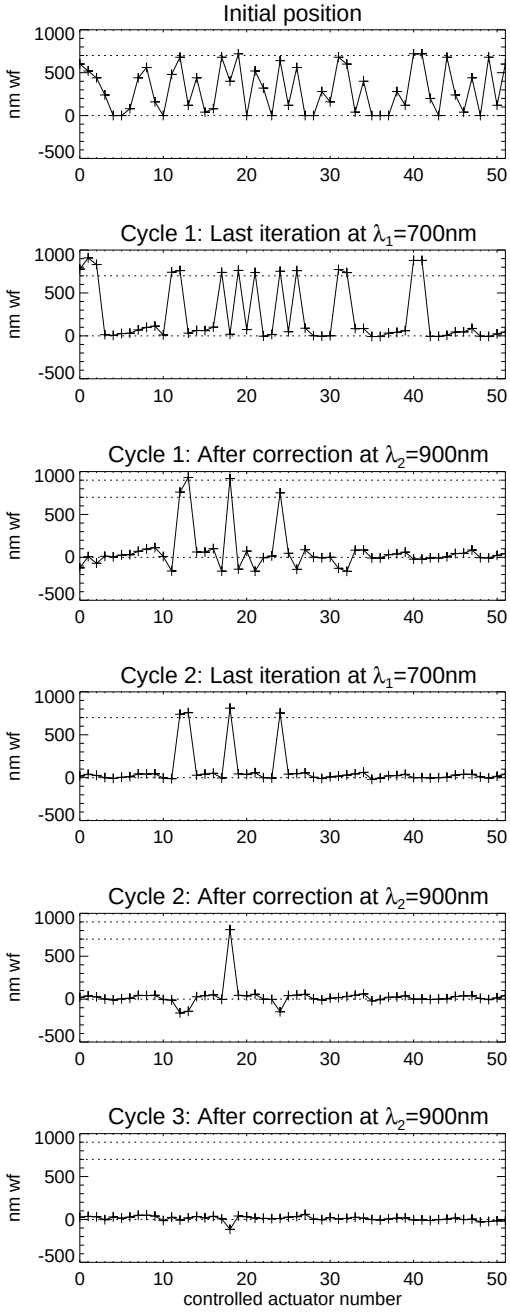

Figure 3.15: Multi-wavelength experiment results. Each of the plot represent the mirror segment configuration at different steps of the phasing procedure.

- single layer turbulence with an equivalent seeing of $0.6''$ for a $8\,m$ pupil
- gain of the integrator -0.7
- tip-tilt modulation $4\lambda/D$
- the Low-Order Removing (LOR) filtering technique (described in sect. 5.1.2) was applied filtering the first 3 Zernike modes in the PYPS signal space
- exposure time: $36\,s$
- binning mode: 1X1 [6]

A full calibration (following the procedure described in sect. 3.2.2) was performed at each wavelength (λ_{CL} and λ_{OL})prior to the multi-wavelength experiment. A total of six cycles were performed. Fig. 3.15 summarizes the experimental results for the first three cycles. The plots show the piston values (nm wavefront) of the 52 controlled actuators. From top to bottom are represented the initial actuator position, then the configuration reached after the first closed-loop operated at λ_{CL}. The dotted lines represent the zeros stable points for the closed loop that are $\Delta\phi = 0$ and 2π. After this first piston correction 14 actuators result phased around the 2π position. Then the piston measurement is performed at λ_{OL} and 10 of the 14 unphased segments are recognized and corrected. A second and a third identical cycle are performed driving all the actuator around the $\Delta\phi = 0$ position. Other three (not represented in fig. 3.15) have been performed testing successfully the multi-wavelength procedure stability. The achieved residual piston error is still limited by the mirror step resolution of $20\,nm$ wavefront.

[6] At the acceptance test, the CCD camera was not able to properly operate the other binning modes.

3.2.5 Wavelength Sweep preliminary test

During the work done in preparation to the acceptance test, we performed some test as conceptual proof of the Wavelength Sweep Technique (WST) illustrated in sect. 2.3.3. A liquid tunable filter (mod. SNIR produced by

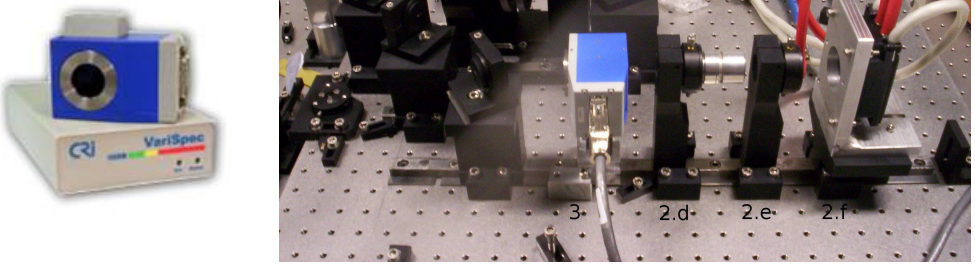

Figure 3.16: **Left:** the liquid crystal tunable filter used in the experiment. The device lies on its small control electronic box. **Right:** the tunable filter (in blue) mounted on the PYPS board.

LOT-Oriel) has been integrated in the PYPS optical train as reported in fig. 3.16. The main characteristics of this device are:

- working range $650 \div 1100\,nm$ (used up to $950\,nm$ because od the CCD quantum efficiency limit)
- bandwidth $10\,nm$
- field of view 7.5^o
- wavelength selection accuracy $< 1\,nm$

- settling time 150 ms

We verified the WST validity measuring the phase steps on the MEMS segment edges. We repeated the measurement on 20 segments and at different step values up to the DM limit of 2.5 μm wavefront. Fig. 3.17 shows the comparison between the WST results and those obtained with an independent phase step measurement. These measurement validate the WST concepts reaching an accuracy of 200 nm. Further details and results can be found in [42], where the complete phasing algorithm for the WST has been developed and tested with numerical simulation. This work is done in preparation for

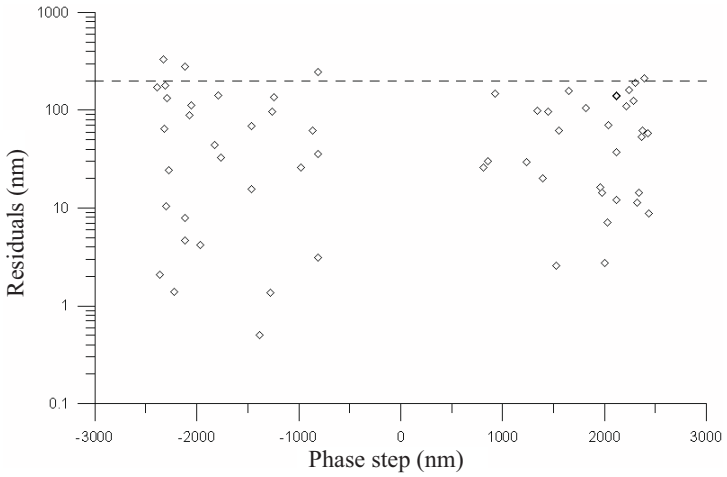

Figure 3.17: The difference between the single step measured with the WST and the reference measurement. This residual is plotted as function of the step amplitude. The dotted line defines the 200 nm level, considered the achieved accuracy in this test.

the experiment foreseen in 2008 at WHT (sect. 4.4), were the technique will be tested with the $\pm 4\,\mu m$ physical stroke of the NAOMI DM (sect. 4.1).

Chapter 4

Pyramid co-phasing at WHT

The William Herschel Telescope (WHT) is a $4.2\,m$ diameter optical/IR instrument located at the Roque de los Muchachos in the La Palma island (Canary - Spain) and managed by the Isaac Newton Group (ING). The WHT is equipped with an adaptive optics system [43], called NAOMI (fig. 4.3). The relevance of this telescope in co-phasing comes out from the NAOMI deformable mirror (DM) that is composed by 72 square segments controllable in tip, tilt and piston. As required for the single conjugated adaptive optics systems, this corrector is conjugated to the atmospheric ground layer, that is optically equivalent to the telescope pupil. Moreover each of the 6 segments present across the pupil, scaled on the $4.2m$ of the primary mirror, have an equivalent side length of $0.7\,m$. Therefore, the beam available on the NAOMI bench is optically equivalent to the beam provided by a telescope with a segmented primary mirror composed by segments having approximately the same size foreseen for the E-ELT and TMT ($1.4\,m$ in both telescopes). In addition, the Isaac Newton Group is promoting the WHT as testbench for the development of the new technologies required by the ELTs [44], as the laser guide star adaptive optics systems [45] and co-phasing. In

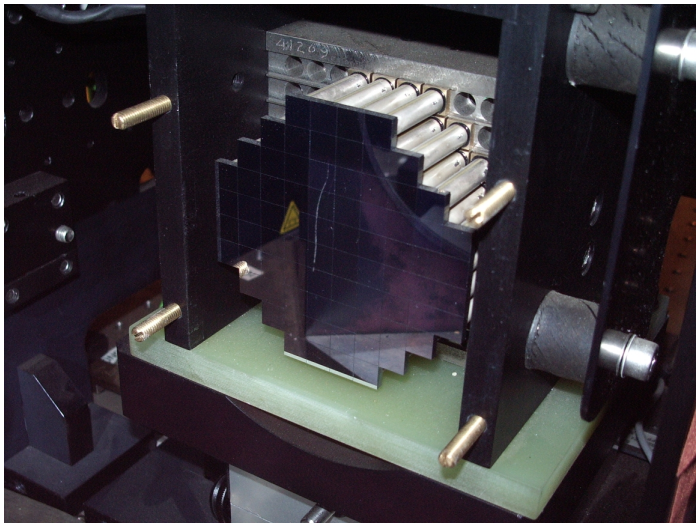

Figure 4.1: the NAOMI deformable mirror.

this framework, the Arcetri Adaptive Optics Group started in 2004 a collaboration with the ING and the Durham University (responsible for NAOMI). This collaboration is aimed to develop and test the Pyramid Phasing sensor at WHT. In the following sections we will illustrate the setup and the main results achieved in the co-phasing experiments held at WHT.

4.1 The experimental setup

The WFS tested at WHT is a PYPS prototype having similar design to the final APE unit (sect. 3.1). The optical configuration and functionalities of this sensor are equivalent to those of PYPS for APE exposed in sect. 3.1. A small sketch of the WFS ca be find in fig. 4.3. The coupling with the NAOMI optical train has been relatively simplified thanks to the system location at one of the Nasmyth focal stations (fig. 4.2). Removing the pick-up used to feed the NAOMI WFS, a f_{15} telecentric beam is available on the bench. Using a simple refocusing system, composed by two lenses and two

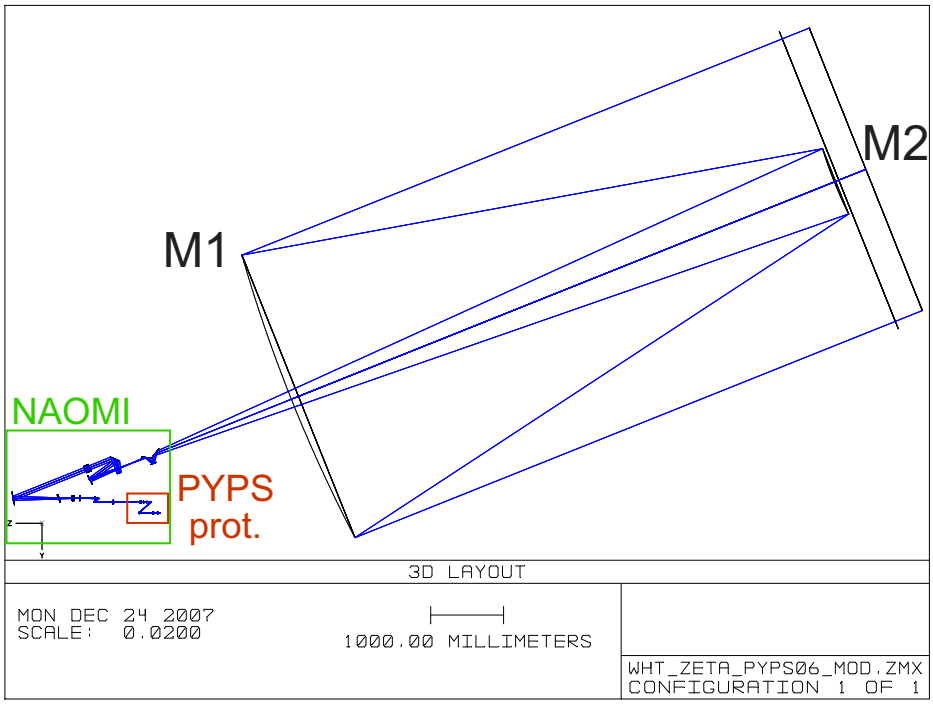

Figure 4.2: The optical configuration of the WHT with the 4.2 m primary mirror (M1), its secondary (M2) and the NAOMI adaptive optics system at a Nasmyth focus (the flat tertiary mirror is not represented in this sketch). The PYPS prototype has been arranged on the NAOMI bench as described in the text and shown in fig. 4.3.

plane mirrors, the PYPS prototype has been accommodated at the NAOMI optical train, as shown in fig. 4.3.

The electronic part of the setup was composed by two commercial Linux-PC: the first was dedicated to the CCD frame acquisition and the fast-steering mirror control; the second was the real-time computer devoted to the signal computation and reconstruction multiplication. All the communication in between the two PCs and the DM electronic has been realized with the TCP-IP protocol and via ethernet connection.

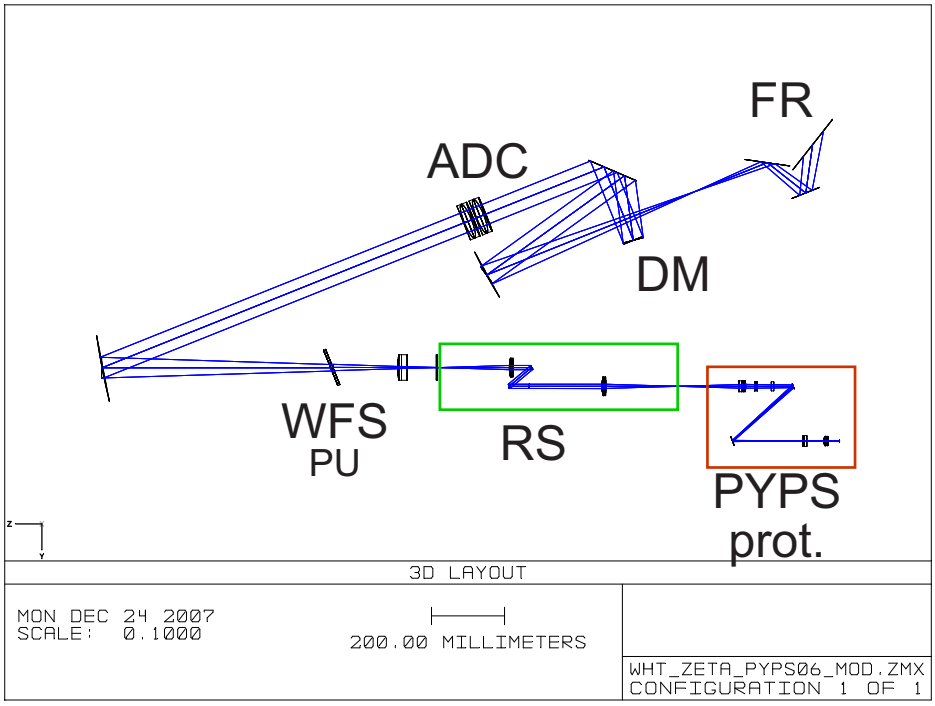

Figure 4.3: The NAOMI system. The main parts are the deformable mirror (DM), the atmospheric dispersion corrector (ADC), the field rotator (FR) and the WFS pick-up (WFSpu), removed in order to feed the PYPS prototype. The focus plane of the available beam is placed inside a mechanical structure, resulting not accessible. A small refocusing system (RS) has been setup in order to accommodate the phasing sensor (PYPS prot.) in the optical train.

4.2 First mirror flattening

The first step, in order to run the co-phasing closed loop, is to perform the system calibration, as done for the APE's PYPS in the acceptance test (sect. 3.2.2) and described in sect. 2.2.3. We remind that the main calibration phases are: the pupil acquisition, the interaction matrix M and slope-null

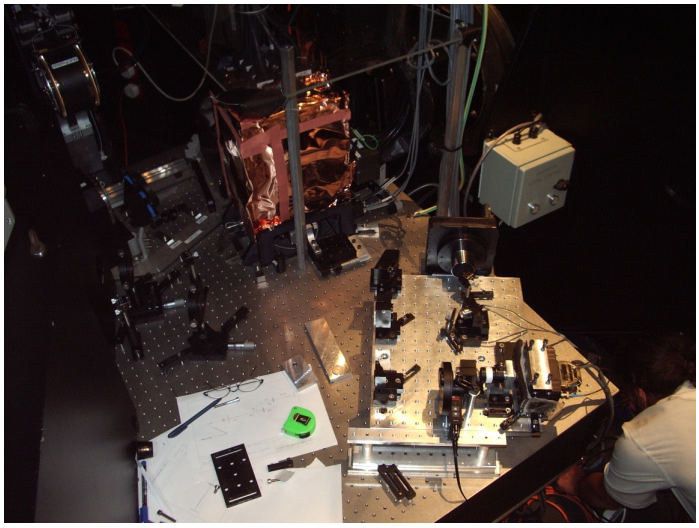

Figure 4.4: The PYPS prototype hosted on the NAOMI bench at the Nasmyth focus of the WHT.

vector $\mathbf{S_0}$ measurements. These last two steps theoretically would demand a perfectly phased and aligned (flattened) mirror. Considering M, that is because the piston signal, in the reconstruction process (sect. 2.2.3), is linearized with the slope $\Delta\mathbf{S}/\Delta\mathbf{C}$, where $\Delta\mathbf{S}$ is the difference in signal obtained applying the command difference $\Delta\mathbf{C}$; if, as example, M is acquired applying $\pm\Delta C/2$ starting from $\Delta\phi = \pi$ the measured slope has opposite sign creating a diverging loop. Considering $\mathbf{S_0}$, the flattened mirror should be required because it represents the position we want to restore with the closed loop operation. Therefore, the first step at WHT, as with a real segmented primary, became providing a first mirror flattening with PYPS itself.

Let's first establish the required accuracy for this first phasing in the context of our experiment, that is demonstrating the PYPS ability to control piston and tip&tilt of a segmented mirror. We assume now acquiring M and S_0 for a single segment when is out of phase of $\Delta\phi_0$. That means, first, the loop will drive this actuator to $\Delta\phi_0$ because $\mathbf{S_0} = \mathbf{S}(\Delta\phi_0)$. This is

a systematic error that can be taken into account without compromise the demonstration of the PYPS phasing ability. The critical effect, as said, is on M, where we need to keep $\Delta\phi_0$ in the range $[-\pi/2, +\pi/2]$ to preserve the correct sign, but also we want $|\Delta\phi_0| \ll \pi/2$ because $M = 0$ when $\Delta\phi_0 = \pi/2$. Of course, we will obtain the best PYPS performances for $\Delta\phi_0 = 0$, but the PYPS sensitivity ($\partial S/\partial(\Delta\phi) \propto \cos(\Delta\phi)$) will be decreased less than 15% for $|\Delta\phi_0| < \pi/6$. We can keep this as requirement for our first flattening for the WHT experiment, that, working with a $700\,nm$ wavelength, translates in $\sim 60\,nm$ accuracy on the wavefront. The first phasing has been obtained with PYPS itself using the Segment Sweep Technique (described in sect. 2.3.2). A semi-automatic software tool has been developed for the SST use (a screen-shot is reported in fig.4.5). This procedure is taking one segment as reference and then sweeping the neighbors through a $\pm 1.5\mu m$ range. A sub-aperture is found on the edge between the reference segment and the sweeping one. The signal of this sub-aperture is then plotted and the phased position determined as the middle between the main maximum and minimum. Afterward a second, finest sweep is performed around the estimated physical zero in order to achieve the required accuracy. The segment is moved to the estimated position and considered as phased. In the next step the segments adjacent to a phased one can be sweep. Iterating this procedure, a set of 13 segments of the NAOMI DM has been phased, using a bandwidth of $300\,nm$ centered on $700\,nm$. We can estimate the phasing accuracy considering that in the finest sweep, limited in the range $\pm\lambda/4$, is composed by at least 10 steps. Therefore, the resulting accuracy is $\sim 35\,nm$ on the wavefront. This value is in the specific we had for an effective interaction matrix acquisition and can be reduced increasing the step sampling.

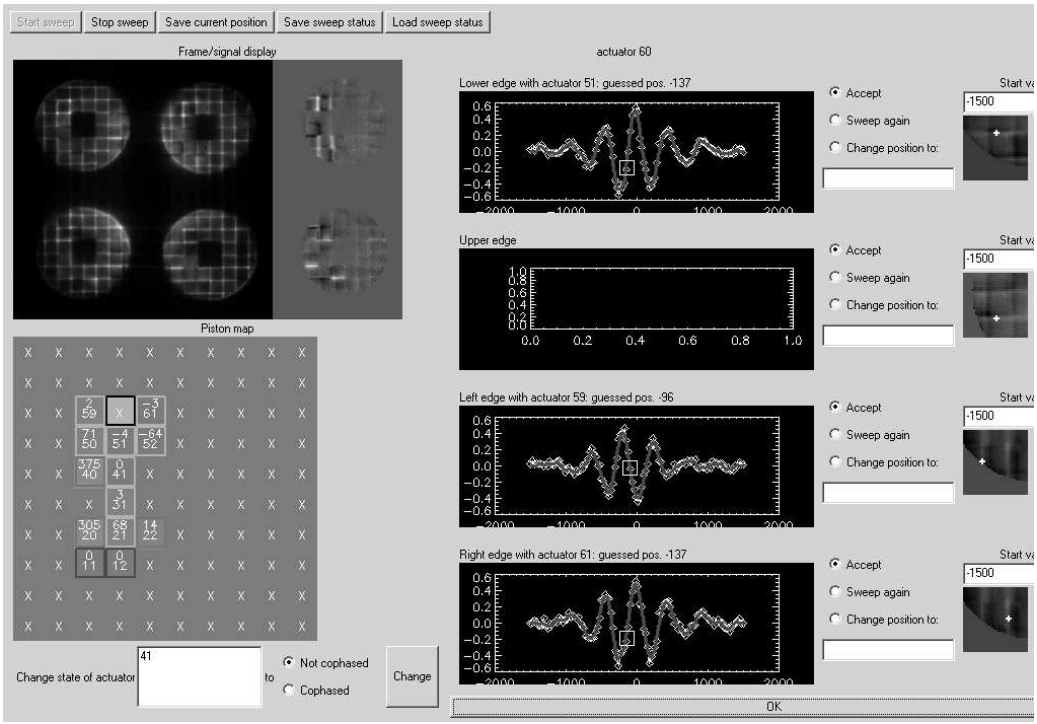

Figure 4.5: A screen-shot of the SST software tool during the operation. In the left upper corner the PYPS frame and real time signals are shown. In the left bottom corner there is a schematic representation of the mirror segment status (phased, un-phased, or sweeping), these status can be changed by the user. On the extreme right column the selected edge sub-apertures are shown, while the graphs show the corresponding signal plot during the segment sweep. The phased edge position is estimated looking to the absolute maximum and minimum positions.

4.3 Calibration and closed loop operations

The achieved first phasing allowed to acquire $\mathbf{S_0}$ and M for the phased set of segments. Fig. 4.6 shows an example of the obtained M. This is the first experimental result showing an interaction matrix for PYPS with piston and

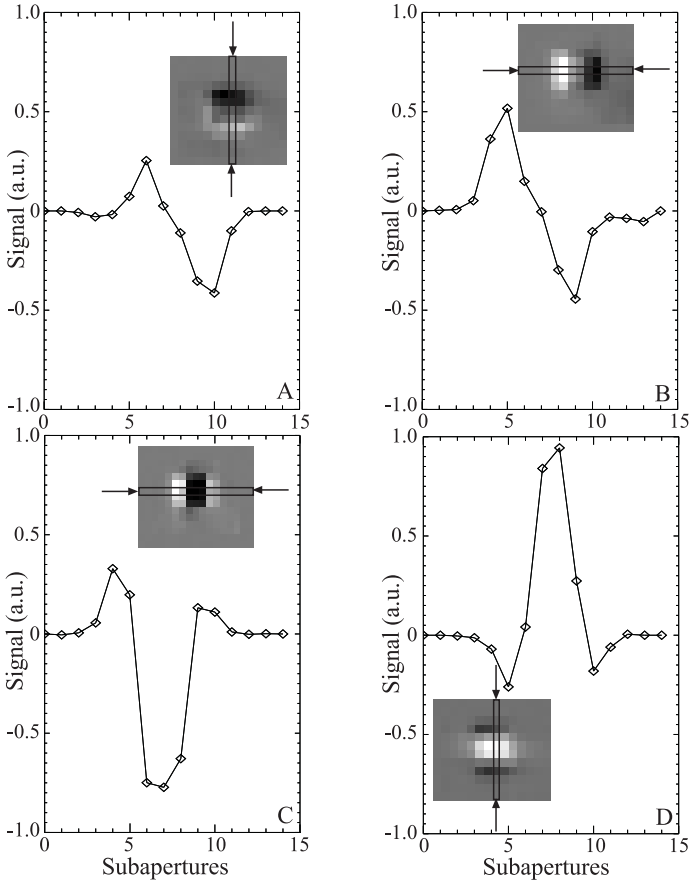

Figure 4.6: Plot and bi-dimensional insets of the PYPS signals, corresponding to (A, B) Y and X piston signals and (C, D) X tip and Y tilt. The bi-dimensional insets show the patch of the pupil containing the considered segment and the signal patterns.

tip&tilt. The measured signals confirmed the theoretical analysis and numerical simulation illustrated in sect. 2.1. We start our correction loop after placing the mirror in a perturbed position. Typical figures for the piston, tip, and tilt wavefront perturbations are $100\,nm$ for the piston and $300\,nm$ for the tip and tilt, peak to valley. This values are choose in order to not introduce wavefront steps larger than the capture range in single wavelength

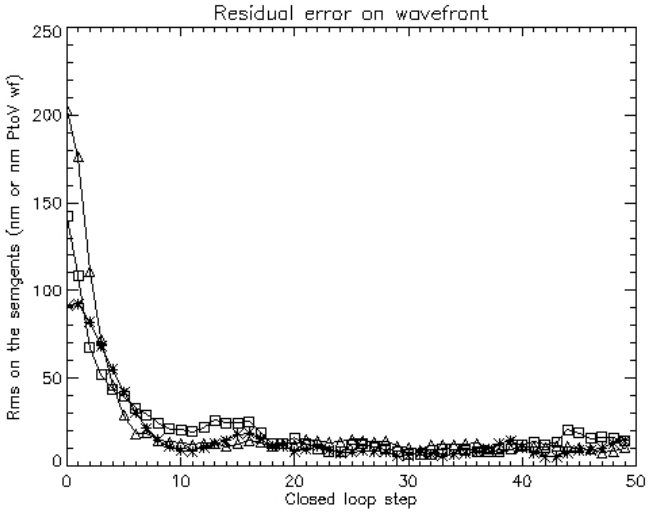

Figure 4.7: An example of mirror phasing and alignment taken from the July 2005 run. The plot reports piston (asterisk), tip&tilt rms on the 13 controlled segments of the NAOMI DM during the close loop operation. Mirror flatness achieved is about 5nm and 10nm for piston and tip&tilt respectively.

discussed in sect. 2.3. Then we run the closed-loop operation as described in sect. 2.2.3. In fig. 4.7 is shown a typical loop correcting piston and tip&tilt on the 13 controlled segments. The zero position for piston and tip&tilt is represented by the mirror command set corresponding to the recorded $\mathbf{S_0}$. The result shown in fig. 4.7 demonstrated, for the first time, the ability of a pyramid wavefront sensor to correct simultaneously in closed-loop piston and tip&tilt of the controlled segments. This experiment has been run feeding the optical system with an artificial source and without any turbulence disturbance (real or simulated). The phasing and aligning correction achieved a stable closed-loop with an accuracy of less than $10\,nm$ wavefront for both piston and tip&tilt.

4.4 Next future for co-phasing at WHT

The obtained results encouraged a follow-up for the co-phasing experiments at WHT. This has been formalized in a collaboration in between INAF (Osservatorio di Arcetri) and the Durham University and has been funded by PPARC. This project foresee the upgrade of the PYPS prototype and a more complex opto-mechanical interface for its installation at the NAOMI bench. Four half nights at WHT has been allocated to the co-phasing experiment in January 2008. The main goal of this experimental run are:

1. the test on-sky of the co-phasing correction using a natural guide star as reference source experiencing the real atmospheric disturbance;

2. the test of the Wavelength Sweep Technique (see sect.2.3.3) implementing a liquid crystal tunable filter in the PYPS optical train

3. the most challenging goal is the realization of the adaptive optics and co-phasing correction, obtained both simultaneously with the PYPS prototype and the NAOMI DM.

Chapter 5

Towards to the ELT's co-phasing

In the previous chapters we illustrated the main part of the PhD work devoted to the study, design, realization and experimental characterization of PYPS. In the present chapter we discuss two subjects conceived while developing and testing the phasing sensor. Both arguments are aimed to improve the technique for the real ELT co-phasing.

5.1 Improving the seeing-limited co-phasing

As stated in sect. 1.2.2, the baseline strategy for the ELT's phasing sensors is working in seeing-limited condition allowing the telescope phasing without the needing of other devices as adaptive optics systems. In *seeing-limited* conditions the PWFS measurements will be affected by the atmospheric turbulence. In principle, it is possible to *average out* the phase perturbations introduced by the atmospheric turbulence using an exposure time (T_e) much larger then the atmospheric coherence time. In this chapter we present two

spatial filtering techniques aimed to reduce the impact of atmospheric perturbations. These techniques have been validated experimentally with PYPS (see chapter 3).

5.1.1 Interaction Matrix Masking

The first technique presented here is called *Interaction Matrix Masking* (IMM). In this case the Interaction Matrix (M) measurement is assumed to be done on sky. The residuals of the time averaged atmospheric disturbance are seen as noise in the M measurements and corrupt its pseudo-inverse R used for wavefront reconstruction. It is important to note that, as shown in sect. 2.1.1, the signal produced by the differential pistons between a given segment and its neighbors is *well localized* on the corresponding edges; on the contrary, the signal produced by the turbulence perturbations is *wide spread* over the whole system pupil. The IMM consists in applying a mask on each of the signals recorded in the M; the mask values are 1 in a square area centered on the considered segment and 0 elsewhere, as shown in fig.5.1. This masking technique permits to remove most of the residual signals produced by the atmospheric turbulence (or other spurious signals) from M prior to the computation of its generalized inverse $R = M^{+}$.

In addition, the use of this masking technique enables to perform a *parallel* M acquisition. That is, the PWFS signals related to all *non-contiguous* segments can be recorded at the same time and split a-posteriori using the corresponding masks. In such a way, the M acquisition time depends only on the segments geometry and no dependence exist on the number of segments. In fact, this approach allows the M on-sky acquisition for the ELTs.

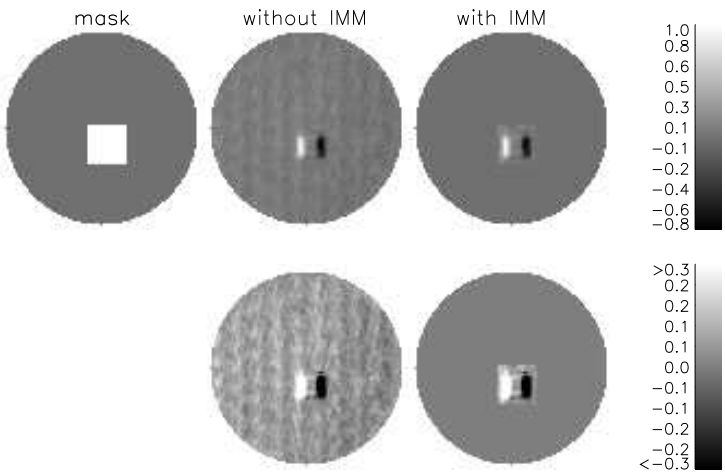

Figure 5.1: Example of a mask applied in M (top-left). PYPS signal ($\mathbf{S_x}$), in arbitrary units, obtained when a piston is applied to a central MEMS segment with (top-right) and without (top-center) the IMM applied. The same signals are represented in a reduced signal range (bottom).

5.1.2 Low Order Removing

The second spatial filtering technique we present is called Low Order Removing (LOR). It is applied during the closed-loop operation of the co-phasing system. It is still based on the fact that the phase discontinuities introduced by the mirror segmentation produce high-spatial-frequency signals[1], whereas the phase errors introduced by the atmospheric turbulence produce signals that are dominant at lower-spatial frequencies. In principle, all the turbulence contribution having a spatial order lower than the one introduced by the mirror segmentation, f_M, could be filtered out at each closed-loop iteration. Also, note that the (remaining) turbulence high-spatial frequencies,

[1]That is because there will be tens of segments on the diameter of the ELT primary mirror and the signal is localized on the segments edges. Therefore the spatial frequencies of interest are around $1/d$, where d is the segment size.

because of their shorter correlation times, require a smaller time to be averaged out. Therefore, the exposure time T_e could be effectively reduced up to the value required to average out the spatial frequencies of the order of f_M. In the PYPS case, as demonstrated by eq. 1.5, for continuous aberrations, the signals are proportional to the first derivative of the wavefront with respect to the two orthogonal directions (x, y) in the pupil plane. Therefore, we propose to implement the second spatial filtering technique by removing the lower spatial frequencies directly in the PYPS x and y signal spaces. Following a modal approach, we choose to remove the first n_z Zernike polynomials from the PYPS signals (where $n_z = 1$ is the piston). Denoting the signal vector as $\mathbf{S} = [\mathbf{S_x}; \mathbf{S_y}]$, the reference position vector as $\mathbf{S}_0 = [\mathbf{S_{x_0}}; \mathbf{S_{y_0}}]$, and the *Zernike-removed* signal vector as $\mathbf{S}_{zr} = [\mathbf{S_{x_{zr}}}; \mathbf{S_{y_{zr}}}]$, the first n_z Zernike modes can be removed from the **x**-component of the signal vector, $\mathbf{S_x}$, at each closed-loop iteration simply as:

$$\mathbf{S_{x_{zr}}} = \left[I - P_z \left(P_z^T P_z \right)^+ P_z^T \right] \left(\mathbf{S_x} - \mathbf{S_{x_0}} \right) \tag{5.1}$$

where P_z denotes a projection matrix containing the first n_z Zernike modes defined on the pupil, and I denotes the identity matrix. The same filtering procedure applies to the **y**-component of the signal vector, $\mathbf{S_y}$.

5.1.3 Experimental results and discussion

Both filtering techniques have been tested in the Arcetri laboratories whith PYPS and the setup used for the acceptance test described in sect. 3.2. In the experiment the 50 controlled MEMS's segments have been set to a random piston configuration having a distribution of $180\,nm$ peak-to-valley and $54\,nm$ rms on the mirror surface. Then, the closed-loop correction is done. The effects of IMM have been tested, as reported in fig.5.2, at $T_e = 72s$

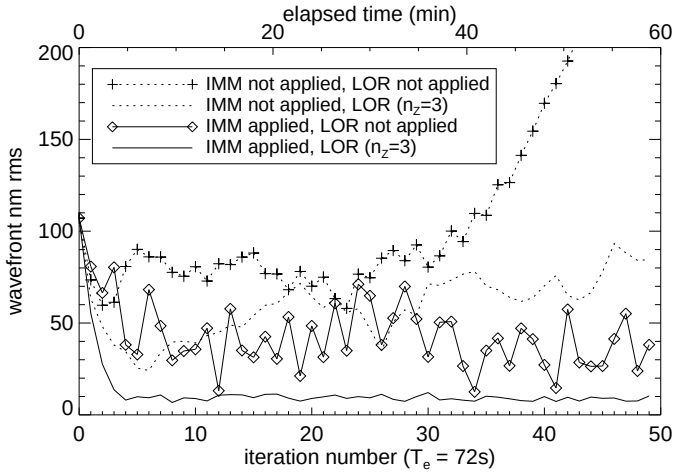

Figure 5.2: The piston error rms of the 50 controlled segments as function of the closed loop iterations for $T_e = 72s$ and $n_z = 0$ and 3 in the cases with and without IMM. The single segment error is computed as difference between the MEMS iteration command and the reference one.

with ($n_z = 3$) and without LOR ($n_z = 0$). In both cases the reconstructor obtained with the masked M showed improved performances, allowing the loop convergence for $n_z = 0$ and reducing the residual piston rms from $64\,nm$ up to $10\,nm$ on the wavefront for $n_z = 3$.

The LOR technique has been tested closing the loop in three different filtering conditions: without LOR ($n_z = 0$), with the first three ($n_z = 3$) and the first six modes removed ($n_z = 6$). All the three cases have been repeated for three different exposure times $T_e = 6\,, 36$ and $72\,s$; the measurements results are reported in fig.5.3.

We define here the phasing time $T_p = T_e \cdot N_{it}$ where N_{it} is the number of iteration required for convergence. For all successful correction sequences we found $N_{it} = 6$. To quantify the improvement in phasing time

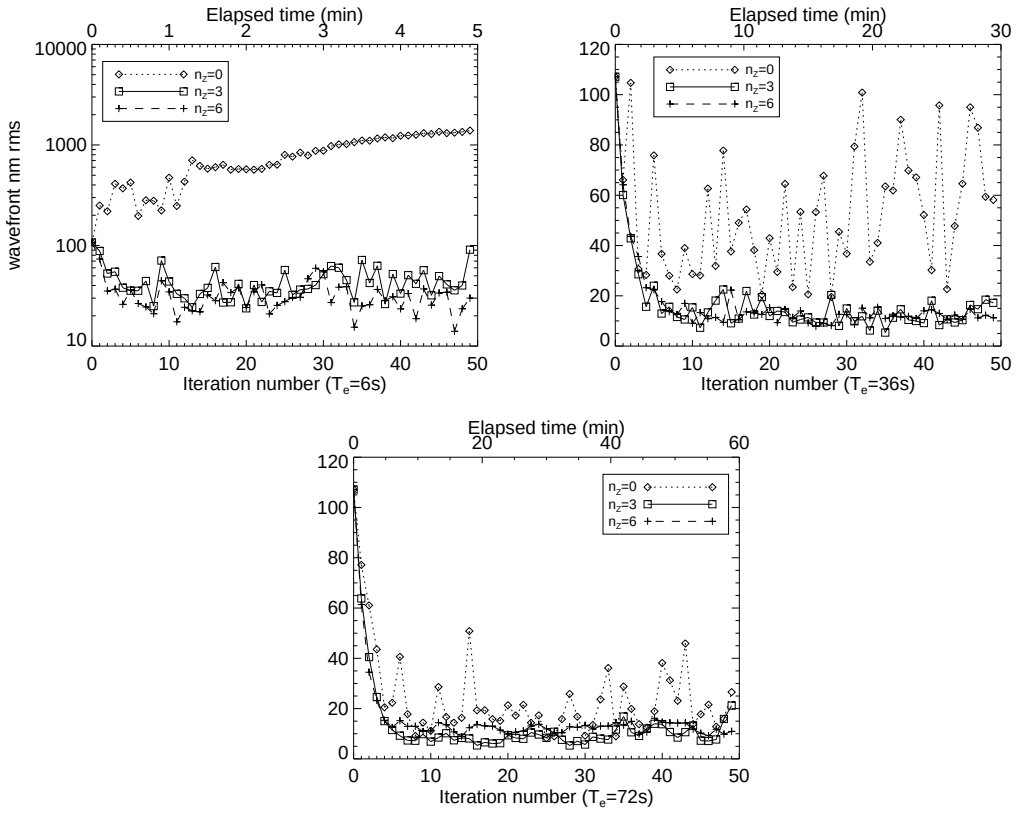

Figure 5.3: The LOR test in closed-loop. The plots, as in fig.5.2, represent the residual pistons vs the loop iterations in several filtering and integration conditions:$T_e = 6\,s$ (**top-left**), $36\,s$ (**top-right**) and $72\,s$ (**bottom**). IMM is applied in all the loops.

due to the IMM plus LOR , we consider the results reported in fig.5.4. The residual achieved for $T_e = 6\,s$ case and filtering techniques ($30\,nm$) is comparable with the residual achieved with $T_e = 72\,s$ of integration without LOR ($20\,nm$). T_p in the above are 0.6 and $7.2\,min$ respectively, so measured gain in T_p is a factor 12. This result applies to the ELT case, considering that the the effective segment size in the experiment is $0.9\,m$ so similar to the currently segment size in the ELT project. Moreover the Pyramid

Sensor measure all the segments at the same time so that T_p will not depend on the number of segment. Now we note the following: because of the periodical behavior of the turbulence introduced by the rotating plate (see sect. 3.2.1), the time-averaged phase perturbation residuals (Φ_{rp}) scales as $1/T_e$. On the contrary, the time-averaged phase perturbation residuals in the real atmosphere (Φ_a) scales as $1/\sqrt{T_s}$ where T_s is the exposure time on sky (when T_s is large compared to the coherence time). So, to reach on sky the same residual reduction $R = \Phi_{rp}[1]/\Phi_{rp}[2] = T_e[2]/T_e[1]$ obtained in lab with long ($T_e[2]$) and short ($T_e[1]$) exposures, we need to satisfy the equation $R = \Phi_a(T_s[2])/\Phi_a(T_s[1]) = \sqrt{T_s[2]}/\sqrt{T_s[1]}$. That means $T_s[2]/T_s[1] = (T_e[2]/T_e[1])^2$ that translates, in our experiment, in about a factor 100 in T_s. This dramatically reduces the time required for ELTs primary phasing. Moreover, in the real atmosphere case, this gain in T_e is crucial for the loop stability because reduces the probability of events that compromise the real turbulence average (i.e. r_0 fluctuations and wind direction changes). The same plot (fig.5.4) suggests another consideration: we note that, for $T_e = 36$ and $72\,s$, the performances for $n_z = 3$ and 6 are similar, while, for $T_e = 6\,s$, the loop performances are improved for $n_z = 6$ respect to $n_z = 3$. This is in agreement with the comment previously stated that the integration time T_e required to average out the atmospheric perturbation is reducing with the increasing of the spatial frequencies.

A more detailed study of the filtering performances will be done during the test on the APE bench (sect. 1.3) at UT3 of the VLT, and at the William Herschel Telescope, during the next experimental run (sect. 4.4). In both experimental environments the techniques will be performed at the telescope with a natural guide star experiencing the real atmosphere.

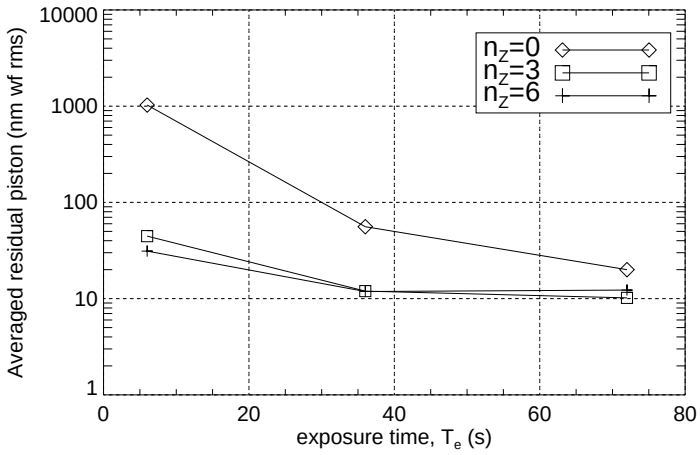

Figure 5.4: In this plot are compared the performances of the closed loop in all the T_e and n_Z conditions experimented. In the vertical axis are reported the residual piston values (rms on the 50 actuated segments) averaged on the iterations $20 - 50$.

5.2 Double segmentation co-phasing

The increased dimension of the primary mirror of the ELTs also implies to have larger sizes of the other optics of the telescope optical train. Some optical design, as the E-ELT one, foreseen the presence of large adaptive optics corrector (M4). The realization of monolithic large deformable mirrors is critical and very expensive; so, the segmentation of this device is a solution considered and advantageous. Of course, a second segmentation introduce the problem of the phasing of a double segmented optical train. Here below we present the results of a preliminary study aim at demonstrate that a single pyramid wavefront sensor is able to simultaneously control in closed-loop piston and tip&tilt of the segments of 2 segmented mirrors in the same optical train. Figure 5.5 shows the simplified geometry considered in this study,

where the two mirrors are supposed both plane and in the system pupil. The primary mirror is formed by 15x15 square segments whereas the secondary mirror is formed by 3x3 square segments. The only source of error that has been considered in this preliminary study is *photon noise*. We will consider three different flux levels (n_{ph}): 1e1, 1e2, and 1e3 photons per sub-aperture. The effect of the CCD RON has been neglected, while the atmospheric turbulence will be studied in a second stage. Considering a primary-mirror segment of $1\,m$ side, 1 second of integration time, and a sensing bandwidth of $300\,nm$, these flux levels are equivalent to star magnitudes in R band of 18.5, 16.0 and 13.5 respectively. Each primary segment is sampled with 6x6 PYPS

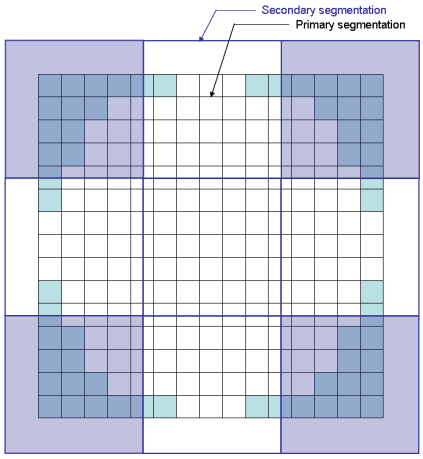

Figure 5.5: A sketch of the considered geometry, showing the segmented patterns of both primary and secondary segmented mirrors superposed in the the telescope pupil. The shaded segments are the ones out (or partially out) of the circular pupil and so not controlled by the closed-loop.

sub-apertures; consequently each secondary segment is sampled with 36X36 sub-apertures. The wavefront sensing wavelength is set to $\lambda = 632.8\,nm$. The interaction matrix (see sect.2.2.3) has been acquired simply adding the

piston and tip&tilt of the secondary mirror as further degrees of freedom to be controlled.

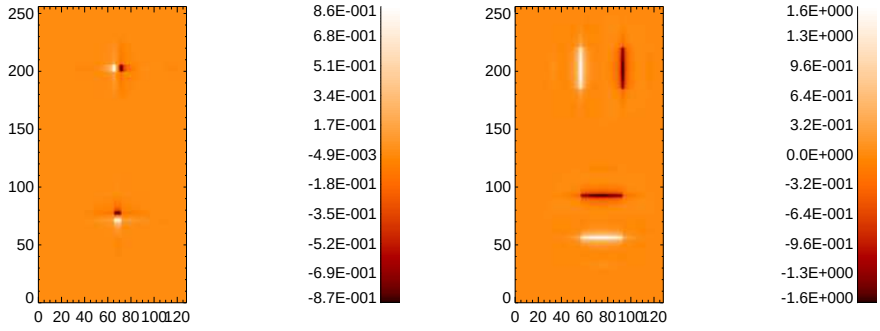

Figure 5.6: Normalized pyramid WFS signal corresponding to a piston signal of: *(Left)* a central segment of the primary mirror; *(Right)* the central segment of the secondary mirror.

An example the interaction matrix (IM) columns for primary and secondary segment piston are reported in fig. 5.6, where each signal column is represented in 2D in order to show the spatial signal pattern. The working principle for the disentangling between primary and secondary mirror segments is the same discussed in 2.2.1 that allows to disentangle the piston and tip&tilt signals. That is the orthogonality, in the signal space, of the IM columns produced by each single degree of freedom of the system. The geometrical arrangement represented in fig. 5.5 guarantees the orthogonality of the secondary segment DoF respect to the ones of the primary, that is because the secondary segment edges are projected in the middle of the primary segment surfaces. This way, is clear that is impossible for a linear combination of piston and tip&tilt of the primary segments to create the signal pattern produced by the secondary segment on the PWFS. This principle can also be applied to different geometries, if the IM column orthogonality

in the signal space is preserved.

The simulated closed-loop started from a position with random errors in piston and tip&tilt in all the segments of both the mirrors (see fig. 5.7). The distribution of the initial errors is again limited ($150\,nm$ rms on the wavefront) by the capture range of the closed-loop operating in single wavelength, as discussed in sect. 2.3. As reference result an equivalent phasing loop has been simulated having only the primary mirror segmented. The comparison between the two loop cases is reported in fig. 5.8 in terms of residual wavefront error in RMS (WFE) and peak to valley (P2V) for each of the 3 considered flux levels. The represented results shows a clear and stable convergence in all the cases. For the single segmentation loops the convergence is reached in less than 10 iterations, while in the double segmentation case this requires between 10 and 15 iterations. The difference between the residual WFEs can easier be appreciated in fig. 5.9 and 5.10. In both plots is evident the expected wavefront residual behavior as $1/\sqrt{n_{ph}}$, while the double segmentation affect the performances only with a lost of less than 3%.

The presented simulation was a preliminary work aimed to prove the concept and give a raw estimation of the double segmentation impact on the residual WFE. This in order to understand if the double (or more generally the multiple) segmentation of the telescope optical train can be an option in the E-ELT design.

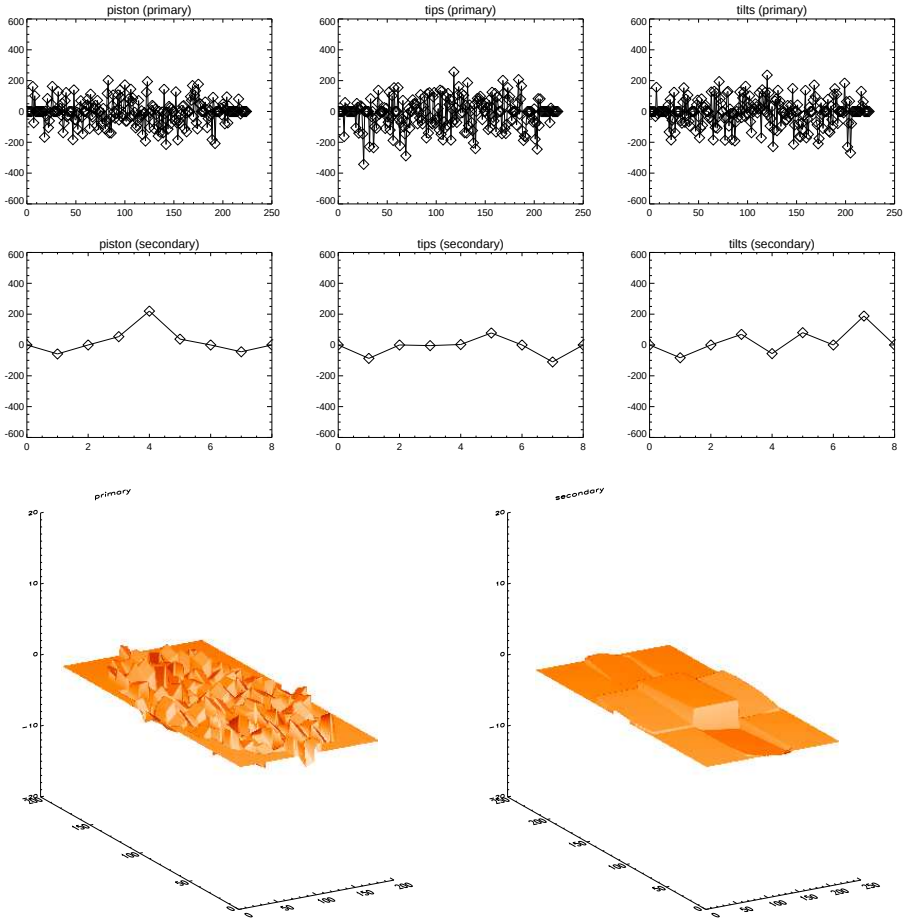

Figure 5.7: **Top:** Piston, tip and tilt coefficients (in nm) corresponding to the initial position of the 225 segments of the primary mirror *and* the 9 segments of the secondary mirror. **Bottom** 3D representation of the primary and the secondary segmented mirrors in their initial positions (in radians).

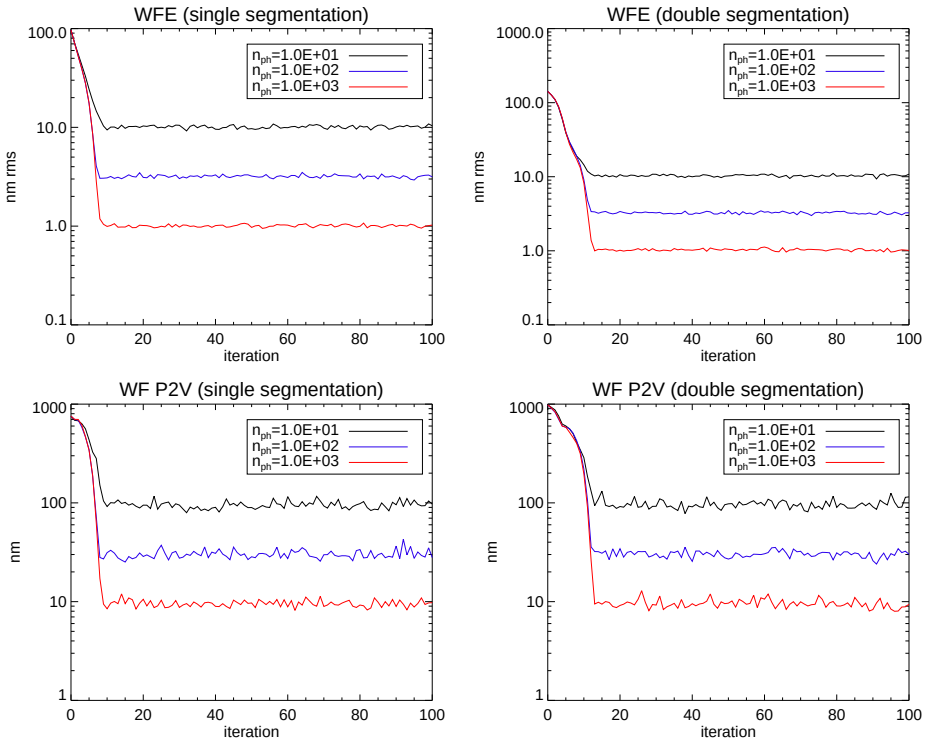

Figure 5.8: Closed-loop evolution of the wavefront error (WFE) for the single (**left**) and double (**right**) segmentation cases. WFE rms (**top**) and peak-to-valley (**bottom**) are represented at each loop step for the three considered cases of photon flux.

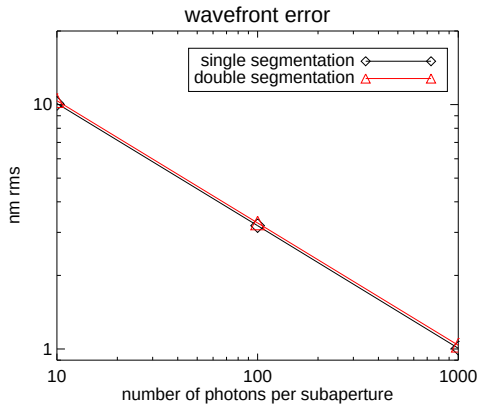

n_{ph} (photons/subaperture)	1e1	1e2	1e3
WFE single segm. (nm)	10.10	3.20	1.01
WFE double segm. (nm)	10.37	3.28	1.04
Relative error (%)	2.67	2.56	2.82

Figure 5.9: Final wavefront error (nm rms) attained for different flux levels in both case studies: single and double segmentation.

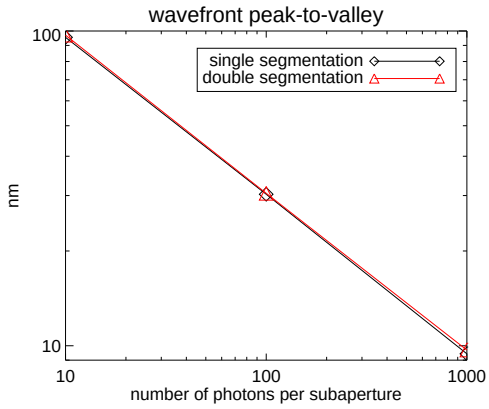

n_{ph} (photons/subaperture)	1e1	1e2	1e3
WFE single segm. (nm)	95.47	30.29	9.43
WFE double segm. (nm)	96.98	30.50	9.69
Relative error (%)	1.59	0.70	2.82

Figure 5.10: Final Peak-to-valley of the wavefront (in nm) attained for different flux levels in both case studies: single and double segmentation.

Chapter 6

Conclusion

The ELT telescope generation will present highly segmented primary mirrors. For such telescopes alignment and co-phasing is a critical task in order to achieve high spatial resolution and high contrast images, but it is also required for all the telescope operations. In this thesis the first pyramid phasing sensor (PYPS) has been designed, realized and tested.

We list below the main achieved results.

- Through analytical computations and numerical simulations we demonstrated the orthogonality of the signals produced by the segment piston, tip and tilt (sect. 2.2.1). This result has been confirmed experimentally (sect. 4.3). The orthogonality in the signal space allows PYPS to **simultaneously control the three degrees of freedom of each segment**.

- The sensor test at William Herchel Telescope (sect. 4.3) demonstrated the PYPS ability to correct piston, tip&tilt achieving a **residual wavefront error** of 1**0 nm rms**.

- The problem of limited capture range for piston detection with monochro-

matic light ($\pm 200\,nm$) has been studied and three different solutions has been proposed. For the multi-wavelength technique case (sect. 3.2.4), laboratory test shows successful closed-loop phasing with initial piston error of $0.8\,\mu m$. For the wavelength sweep technique the capture range is as wide as $\pm 100\,\mu m$ (sect. 2.3.3).

The reached accuracy and capture range satisfies the specifications (sect. 1.2.1) required for the ELT primary mirror phasing and alignment. Moreover the simultaneous control of piston tip&til is a relevant characteristics for the ELT co-phasing. In fact a single wavefront sensor will provide segment phasing and segment alignment.

During the PhD period some other original work has been done on the co-phasing subject. We mention here the two spatial filtering techniques (sect. 5.1) that allow to **reduce the phasing time of a factor 100**, when the sensor is working in seeing-limited mode.

The PYPS characteristics and performances, mainly in terms of accuracy and capture range, will be further investigated in 2008 at ESO-Garching and finally at VLT, during the allocated observing time for the Active Phasing Experiment (sect. 1.3). The pyramid phasing sensor and, in particular, the wavelength sweep technique will be the subject of an observing campaign currently scheduled for April 2008 (sect. 4.4) at the William Herschel Telescope.

Acknowledgments

Ciò che ho imparato in questi anni lo devo principalmente a Simone che mi ha sempre coinvolto nei tanti progetti del gruppo, che mi ha dato fiducia e responsabiltà nel progetto del dottorato, ma mai lasciandomi senza il suo appoggio. Cerca ancora di insegnarmi metodo ed essenzialità, chissà, forse ci riuscirà. Impagabile Armando, che ha sempre tempo e risposte per tutte le domande: dal sensore a piramide alla fisica degli strumenti a fiato. Le sue spiegazioni possono richiedere un paio di lavagnate di equazioni matriciali, ma, se riesci ad arrivare in fondo, sicuramente hai imparato qualcosa. Grazie Piero S. per stimolare quotidianamente curiosità ad *ampio spettro* e lasciare sempre una porta aperta al piano di sopra. Poi è sempre bene ringraziare il capo... ora potresti davvero licenziarmi!

Un grazie importante va al gruppo di persone con le quali ho condiviso gioie dolori e fatiche del progetto: Alfio, Andrea, Fernando e Lorenzo. Non posso certo dimenticare Paolo esempio sempre stupefacente di energia e perseveranza.

Un ringraziamento sentito va a tutto il gruppo AO di Arcetri come insieme perché sono le persone a rendere quell'edificio di cemento un posto dove la mattina si va volentieri lavorare. Non è poco. Grazie quindi anche a chi non ho ancora nominato: Alessandro, Daniela, Francesca, Franco, Iacopo, Luca, Luciano, Marco, Piero R.

Non possono mancare nei miei ringraziamenti tutti i *Chelazzidi*, ovvero coloro che mi hanno sopportato in casa per tutto questo tempo. L'elenco sarebbe davvero lungo, quindi ringrazio esplicitamente coloro che continuano tuttora a sopportarmi: Andrea, Joao (perdona: sono le 3 e non trovo la 'a' giusta), Marco (ti toccano 2 grazie), Pierre e Tiziana. Grazie davvero.

Un grazie speciale ai miei genitori per essere *presenti*, soprattutto nei momenti di bisogno.

Manca solo la persona più speciale, colei che mi è stata vicina anche da $1000Km$. Grazie Ana, ora tocca a te!

Bibliography

[1] J. E. Nelson, "Progress on the California Extremely Large Telescope (CELT)," in *Future Giant Telescopes. Edited by Angel, J. Roger P.; Gilmozzi, Roberto. Proceedings of the SPIE, Volume 4840, pp. 47-59 (2003).*, J. R. P. Angel and R. Gilmozzi, eds., vol. 4840 of *Presented at the Society of Photo-Optical Instrumentation Engineers (SPIE) Conference*, pp. 47–59 (2003).

[2] T. E. Andersen, A. Ardeberg, H. Riewaldt, M. Lastiwka, N. Quinlan, K. McNamara, X. Wang, A. Enmark, M. Owner-Petersen, A. Shearer, C. Fan, and D. Moraru, "Status of the Euro50 Project," in *Ground-based Telescopes. Edited by Oschmann, Jacobus M., Jr. Proceedings of the SPIE, Volume 5489, pp. 407-416 (2004).*, J. M. Oschmann, Jr., ed., vol. 5489 of *Presented at the Society of Photo-Optical Instrumentation Engineers (SPIE) Conference*, pp. 407–416 (2004).

[3] M. Iye and J. Wg, "Concept study of Japan Extremely Large Telescope," in *Ground-based Telescopes. Edited by Oschmann, Jacobus M., Jr. Proceedings of the SPIE, Volume 5489, pp. 417-428 (2004).*, J. M. Oschmann, Jr., ed., vol. 5489 of *Presented at the Society of Photo-Optical Instrumentation Engineers (SPIE) Conference*, pp. 417–428 (2004).

[4] E. T. Brunetto, M. Dimmler, F. Koch, M. Quattri, M. Müller, and B. Sedghi, "OWL opto-mechanics: phase A," in *Ground-based Telescopes. Edited by Oschmann, Jacobus M., Jr. Proceedings of the SPIE, Volume 5489, pp. 571-582 (2004).*, J. M. Oschmann, Jr., ed., vol. 5489 of *Presented at the Society of Photo-Optical Instrumentation Engineers (SPIE) Conference*, pp. 571–582 (2004).

[5] F. W. Kan and J. Antebi, "Giant Segmented Mirror Telescope (GSMT) Structure - A Conceptual Design," in *Future Giant Telescopes. Edited by Angel, J. Roger P.; Gilmozzi, Roberto. Proceedings of the SPIE, Volume 4840, pp. 485-496 (2003).*, J. R. P. Angel and R. Gilmozzi, eds., vol. 4840 of *Presented at the Society of Photo-Optical Instrumentation Engineers (SPIE) Conference*, pp. 485–496 (2003).

[6] D. R. Crabtree, S. C. Roberts, J. T. Fitzsimmons, J. S. Pazder, G. Herriot, M. J. Smith, J. Dunn, and L. K. Saddlemyer, "VLOT: a modest Canadian 20-m telescope," in *Second Backaskog Workshop on Extremely Large Telescopes. Edited by Ardeberg, Arne L.; Andersen, Torben. Proceedings of the SPIE, Volume 5382, pp. 105-114 (2004).*, A. L. Ardeberg and T. Andersen, eds., vol. 5382 of *Presented at the Society of Photo-Optical Instrumentation Engineers (SPIE) Conference*, pp. 105–114 (2004).

[7] R. Gilmozzi and J. Spyromilio, "The European Extremely Large Telescope (E-ELT)," The Messenger **127**, 11–+ (2007).

[8] TMT Observatory, "Thirty Meter Telescope, Construction Proposal," (2007).

[9] M. Johns, "The Giant Magellan Telescope (GMT)," in *Ground-based and Airborne Telescopes. Edited by Stepp, Larry M.. Proceedings of the SPIE, Volume 6267, pp. 626729 (2006).*, vol. 6267 of *Presented at the Society of Photo-Optical Instrumentation Engineers (SPIE) Conference* (2006).

[10] G. Chanan, M. Troy, I. Crossfield, J. Nelson, and T. Mast, "The alignment and phasing system for the Thirty Meter Telescope," in *Ground-based and Airborne Telescopes. Edited by Stepp, Larry M.. Proceedings of the SPIE, Volume 6267, pp. 62672V (2006).*, vol. 6267 of *Presented at the Society of Photo-Optical Instrumentation Engineers (SPIE) Conference* (2006).

[11] T. Mast, G. Chanan, J. Nelson, R. Minor, and R. Jared, "Edge sensor design for the TMT," in *Ground-based and Airborne Telescopes. Edited by Stepp, Larry M.. Proceedings of the SPIE, Volume 6267, pp. 62672S (2006).*, vol. 6267 of *Presented at the Society of Photo-Optical Instrumentation Engineers (SPIE) Conference* (2006).

[12] E. Ponslet, D. Blanco, M. Cho, T. Mast, J. Nelson, R. J. Ponchione, M. Sirota, V. Stephens, L. Stepp, A. Tubb, and E. C. Williams, "Development of the primary mirror segment support assemblies for the Thirty Meter Telescope," in *Optomechanical Technologies for Astronomy. Edited by Atad-Ettedgui, Eli; Antebi, Joseph; Lemke, Dietrich. Proceedings of the SPIE, Volume 6273, pp. 627319 (2006).*, vol. 6273 of *Presented at the Society of Photo-Optical Instrumentation Engineers (SPIE) Conference* (2006).

[13] G. Chanan and M. Troy, "Strehl ratio and modulation transfer function for segmented mirror telescopes as functions of segment phase error." Appl. Opt.**38**, 6642–6647 (1999).

[14] D. G. Sandler, S. Stahl, J. R. P. Angel, M. Lloyd-Hart, and D. McCarthy, "Adaptive optics for diffraction-limited infrared imaging with 8-m telescopes." Journal of the Optical Society of America (1917-1983) **11**, 925–945 (1994).

[15] G. A. Chanan, T. S. Mast, J. E. Nelson, R. W. Cohen, and P. L. Wizinowich, "Phasing the mirror segments of the W.M. Keck Telescope," in *Proc. SPIE Vol. 2199, p. 622-637, Advanced Technology Optical Telescopes V, Larry M. Stepp; Ed.*, L. M. Stepp, ed., vol. 2199 of *Presented at the Society of Photo-Optical Instrumentation Engineers (SPIE) Conference*, pp. 622–637 (1994).

[16] G. Chanan, C. Ohara, and M. Troy, "Phasing the Mirror Segments of the Keck Telescopes II: The Narrow-band Phasing Algorithm," Appl. Opt. **39**(25), 4706–4714 (2000).

[17] G. A. Chanan, J. E. Nelson, T. S. Mast, P. L. Wizinowich, and B. A. Schaefer, "W.M. Keck Telescope phasing camera system," in *Proc. SPIE Vol. 2198, p. 1139-1150, Instrumentation in Astronomy VIII, David L. Crawford; Eric R. Craine; Eds.*, D. L. Crawford and E. R. Craine, eds., vol. 2198 of *Presented at the Society of Photo-Optical Instrumentation Engineers (SPIE) Conference*, pp. 1139–1150 (1994).

[18] N. Yaitskova, F. Gonte, F. Derie, L. Noethe, I. Surdej, R. Karban, K. Dohlen, M. Langlois, S. Esposito, E. Pinna, M. Reyes, L. Montoya, and D. Terrett, "The active phasing experiment: Part I. Concept and

objectives," in *Ground-based and Airborne Telescopes. Edited by Stepp, Larry M.. Proceedings of the SPIE, Volume 6267, pp. 62672Z (2006).*, vol. 6267 of *Presented at the Society of Photo-Optical Instrumentation Engineers (SPIE) Conference* (2006).

[19] F. Gonte, L. Noethe, C. Araujo, R. Brast, C. Dupuy, C. Frank, and F. Derie, "Shack-Hartmann sensor for the active phasing experiment," in *Ground-based and Airborne Telescopes. Edited by Stepp, Larry M.. Proceedings of the SPIE, Volume 6267, pp. 626733 (2006).*, vol. 6267 of *Presented at the Society of Photo-Optical Instrumentation Engineers (SPIE) Conference* (2006).

[20] K. Dohlen, M. Langlois, P. Lanzoni, S. Mazzanti, A. Vigan, L. Montoya, E. Hernandez, M. Reyes, I. Surdej, and N. Yaitskova, "ZEUS: a cophasing sensor based on the Zernike phase contrast method," in *Ground-based and Airborne Telescopes. Edited by Stepp, Larry M.. Proceedings of the SPIE, Volume 6267, pp. 626734 (2006).*, vol. 6267 of *Presented at the Society of Photo-Optical Instrumentation Engineers (SPIE) Conference* (2006).

[21] L. Montoya-Martínez, M. Reyes, A. Schumacher, and E. Hernández, "DIPSI: the diffraction image phase sensing instrument for APE," in *Ground-based and Airborne Telescopes. Edited by Stepp, Larry M.. Proceedings of the SPIE, Volume 6267, pp. 626732 (2006).*, vol. 6267 of *Presented at the Society of Photo-Optical Instrumentation Engineers (SPIE) Conference* (2006).

[22] F. Gonté, C. Dupuy, C. Frank, C. Araujo, R. Brast, R. Frahm, R. Karban, L. Andolfato, R. Esteves, M. Nylund, B. Sedghi, G. Fischer,

L. Noethe, and F. Derie, "The First Active Segmented Mirror at ESO," The Messenger **128**, 23–+ (2007).

[23] R. Wilhelm, A. Courteville, S. Estival, A. Bietti, V. Seiller, and F. Gonté, "Shape measurements of a segmented mirror with nanometer accuracy: the APE internal metrology," in *Ground-based and Airborne Telescopes. Edited by Stepp, Larry M.. Proceedings of the SPIE, Volume 6267, pp. 626731 (2006).*, vol. 6267 of *Presented at the Society of Photo-Optical Instrumentation Engineers (SPIE) Conference* (2006).

[24] J. Kolb, S. Oberti, E. Marchetti, and F. Quirós-Pacheco, "Full characterization of the turbulence generator MAPS for MCAO," in *Advances in Adaptive Optics II. Edited by Ellerbroek, Brent L.; Bonaccini Calia, Domenico. Proceedings of the SPIE, Volume 6272, pp. 627258 (2006).*, vol. 6272 of *Presented at the Society of Photo-Optical Instrumentation Engineers (SPIE) Conference* (2006).

[25] S. Esposito and N. Devaney, "Segmented mirror co-phasing using Pyramid Sensor," in *Beyond Conventional Adaptive Optics*, vol. 58 of *ESO Proc.*, pp. 161–166 (2001).

[26] S. Esposito, E. Pinna, A. Tozzi, P. Stefanini, and N. Devaney, "Cophasing of segmented mirrors using the pyramid sensor," in *Astronomical Adaptive Optics Systems and Applications. Edited by Tyson, Robert K.; Lloyd-Hart, Michael. Proceedings of the SPIE, Volume 5169, pp. 72-78 (2003).*, R. K. Tyson and M. Lloyd-Hart, eds., pp. 72–78 (2003).

[27] R. Ragazzoni, "Pupil plane wavefront sensing with an oscillating prism," Journal of Modern Optics **43**, 289–293 (1996).

[28] L. Foucault, "Memoire sur la construction des telescopes en verre argente," Annales de l'Observatoire de Paris **5**, 197–237 (1859).

[29] R. G. Wilson, "Wavefront-error evaluation by mathematical analysis of experimental Foucault-test data." Appl. Opt.**14**, 2286–2297 (1975).

[30] S. Esposito, O. Feeney, and A. Riccardi, "Laboratory test of a pyramid wavefront sensor," in *Proc. SPIE Vol. 4007, p. 416-422, Adaptive Optical Systems Technology, Peter L. Wizinowich; Ed.*, P. L. Wizinowich, ed., pp. 416–422 (2000).

[31] E. Pinna, "Applicazione del sensore a piramide alla misura di discontinuità del fronte d'onda." Università degli Studi di Fienze (2004).

[32] G. Chanan, M. Troy, and E. Sirko, "Phase Discontinuity Sensing: A Method for Phasing Segmented Mirrors in the Infrared," Appl. Opt. **38**(4), 704–713 (1999).

[33] D. L. Fried, "Least-square fitting a wave-front distortion estimate to an array of phase-difference measurements," Journal of the Optical Society of America (1917-1983) **67**, 370–375 (1977).

[34] Golub, G. and Kahan, W., "Calculating the Singular Values and Pseudo-Inverse of a Matrix," Journal of the Society for Industrial and Applied Mathematics: Series B, Numerical Analysis **2**(2), 205–224 (1965).

[35] W. H. Press, S. A. Teukolsky, W. T. Vetterling, and B. P. Flannery, *Numerical recipes in C (2nd ed.): the art of scientific computing* (Cambridge University Press, New York, NY, USA, 1992).

[36] G. Chanan, M. Troy, F. Dekens, S. Michaels, J. Nelson, T. Mast, and D. Kirkman, "Phasing the Mirror Segments of the Keck Telescopes: The Broadband Phasing Algorithm," Appl. Opt. **37**(1), 140–155 (1998).

[37] G. Chanan and A. Pintó, "Efficient Method for the Reduction of Large Piston Errors in Segmented-Mirror Telescopes," Appl. Opt. **43**(16), 3279–3286 (2004).

[38] E. Pinna, S. Esposito, A. Puglisi, F. Pieralli, R. M. Myers, L. Busoni, A. Tozzi, and P. Stefanini, "Phase ambiguity solution with the Pyramid Phasing Sensor," in *Space Telescopes and Instrumentation II: Ultraviolet to Gamma Ray. Edited by Turner, Martin J. L.; Hasinger, Günther. Proceedings of the SPIE, Volume 6267, pp. (2006).* (2006).

[39] S. Esposito, A. Tozzi, A. Puglisi, L. Fini, P. Stefanini, P. Salinari, D. Gallieni, and J. Storm, "Development of the first-light AO system for the large binocular telescope," in *Astronomical Adaptive Optics Systems and Applications. Edited by Tyson, Robert K.; Lloyd-Hart, Michael. Proceedings of the SPIE, Volume 5169, pp. 149-158 (2003).*, R. K. Tyson and M. Lloyd-Hart, eds., pp. 149–158 (2003).

[40] A. Tozzi, "Studio e progettazione di un nuovo sensore di fronte d'onda per il Large Binocular Telescope," in *tesi di Scuola di specializzazione in Ottica*, Università degli Studi di Firenze.

[41] E. Pinna, F. Quirós-Pacheco, S. Esposito, A. Puglisi, and P. Stefanini, "Signal spatial filtering for co-phasing in seeing-limited conditions," Opt. Lett. **32**(23), 3465–3467 (2007).

[42] M. Bonaglia, "Filtro sintonizzabile a cristalli liquidi: un esperimento per il phasing di un ELT." Alma Mater Studiorum - Università di Bologna (2007).

[43] R. M. Myers, A. J. Longmore, C. R. Benn, D. F. Buscher, P. Clark, N. A. Dipper, N. Doble, A. P. Doel, C. N. Dunlop, X. Gao, T. Gregory, R. A. Humphreys, D. J. Ives, R. Østensen, P. T. Peacocke, R. G. Rutten, C. J. Tierney, A. J. A. Vick, M. R. Wells, R. W. Wilson, S. P. Worswick, and A. Zadrozny, "NAOMI adaptive optics system for the 4.2m William Herschel telescope," in *Adaptive Optical System Technologies II. Edited by Wizinowich, Peter L.; Bonaccini, Domenico. Proceedings of the SPIE, Volume 4839, pp. 647-658 (2003).*, P. L. Wizinowich and D. Bonaccini, eds., vol. 4839 of *Presented at the Society of Photo-Optical Instrumentation Engineers (SPIE) Conference*, pp. 647–658 (2003).

[44] R. G. M. Rutten, R. M. Myers, and T. J. Morris, "The 4.2-m William Herschel Telescope as ELT testbed facility," in *The Scientific Requirements for Extremely Large Telescopes*, P. Whitelock, M. Dennefeld, and B. Leibundgut, eds., vol. 232 of *IAU Symposium*, pp. 496–497 (2006).

[45] R. M. Myers, D. B. Calia, N. Devaney, S. Esposito, S. J. Goodsell, A. Goncharov, J. C. Guerra, H. G. de Chatellus, M. A. Harrison, R. Holzloehner, E. Marchetti, T. J. Morris, E. Pinna, J. p. Pique, S. Rabien, M. Reyes, E. Ribak, R. G. Rutten, H. Schnetler, M. Strachan, R. Stuik, and R. G. Talbot, "The European E-ELT WHT LGS Test Facility Consortium," in *Adaptive Optics: Analysis and Methods/Computational Optical Sensing and Imaging/Information Photonics/Signal Recovery and Synthesis Topical Meetings on CD-ROM*, p. AWD5 (Optical Society of America, 2007).